Time-dependent description of the predissociation of N_2^+ in the $C\,^2\Sigma_u^+$ state

B. Paulus,[1] J. F. Pérez-Torres,[1,2,*] and C. Stemmle[1]

[1]*Institut für Chemie und Biochemie, Freie Universität Berlin, Takustraße 3, 14195 Berlin, Germany*
[2]*Departamento de Ciencias Básicas, Universidad de Medellín, Carrera 87 No. 30-65, Medellín, Colombia*

The predissociation of the N_2^+ molecular ion in the $C\,^2\Sigma_u^+$ electronic state through the nonadiabatic coupling with the $B\,^2\Sigma_u^+$ electronic state is studied by solving the Schrödinger equation. The predissociation rates are calculated using Fermi's golden rule and compared with experimental results. We characterize the dynamics by calculating the nuclear probability density $\rho(R,t)$, the nuclear flux density $j(R,t)$, and the two-electron flux density $\mathbf{j}(\mathbf{r}_1,\mathbf{r}_2,t)$. It is found that at the early dynamics, $t \leqslant 100$ fs, Fermi's golden rule breaks down, while a strong correlation between the electronic and nuclear dynamics is observed. Fourier analyses of the probability and flux densities are also presented and yield insight in their frequency dependency.

I. INTRODUCTION

Early investigations (see Ref. [1] and references therein) on radiative decay of vibrational excited levels ν of the $C\,^2\Sigma_u^+$ state of N_2^+ to the electronic ground state,

$$N_2^+(C\,^2\Sigma_u^+,\nu) \rightarrow N_2^+(X\,^2\Sigma_g^+) + \hbar\omega,$$
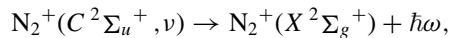
suggested that a predissociative decay,

$$N_2^+(C\,^2\Sigma_u^+,\nu \geqslant 3) \rightarrow N_2^+(B\,^2\Sigma_u^+) \rightarrow N(^4S) + N^+(^3P),$$
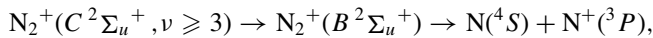
would be 10–200 times more favorable. Subsequent experiments show that the main production of N^+ in the collision of N_2 with He^+ is due to this predissociation [2]. Determination of the ratios of the rates of C-state predissociation to radiative emission obtained for the levels $\nu = 3$–8 confirmed predissociation as the main mechanism of relaxation of the $N_2^+(C\,^2\Sigma_u^+,\nu \geqslant 3)$ [3], thus supporting the early studies [1]. Figure 1 gives a schematic overview of this predissociative mechanism. Direct measurement of the predissociation probability established that levels $\nu \geqslant 3$ predissociate at a rate of about 2×10^8 s^{-1} [4]. A strong isotope effect in the predissociative decay rates was also found [1,5]. The isotope $^{14}N_2^+$ contributes the most followed by the isotopes $^{14}N\,^{15}N^+$ (six times less probable) and $^{15}N_2^+$ (10 times less probable) [1]. Subsequent *ab initio* calculations of predissociative decay rates, or simply predissociation rates k_{ν_C}, were successfully compared with the experimental values [6], reproducing the isotope effect. The same calculations show that the predissociation rates are barely dependent on the rotational quantum number J for the isotope $^{14}N_2^+$, while for the isotopes $^{14}N\,^{15}N^+$ and $^{15}N_2^+$ the k_{ν_C} are strongly dependent on J. Thus, predissociation of $^{14}N_2^+$ can be simulated neglecting the rotational motion without significant consequences on the predissociation rates.

Here we present a detailed theoretical investigation of the predissociation of the rotationless $^{14}N_2^+(C\,^2\Sigma_u^+,\nu)$ system by solving the Schrödinger equation. Recent pump-probe experiments in N_2^+ [7,8] with subfemtosecond time resolution

[8], where predissociation signatures were observed in the kinetic energy release spectrum, motivate this investigation. Thus, pump-probe experiments open the possibility of tracing the predissociation of N_2^+ in time. Therefore we report not only the predissociation rates, but also fundamental quantum dynamical quantities as the time-dependent nuclear probability density $\rho(R,t)$ and the nuclear flux density $j(R,t)$, since these observables can, in principle, be reconstructed from pump-probe measurements, as demonstrated recently [9–11]. Fourier analysis of the probability and flux densities are also presented. Given that the predissociation is dominated by the electronic configurations $2\sigma_g^2 3\sigma_g^2 1\pi_u^4 2\sigma_u^1$ and $2\sigma_g^2 3\sigma_g^1 1\pi_u^3 2\sigma_u^2 1\pi_g^1$ [6], which differ by two molecular orbitals, we calculate the two-electron flux density $\mathbf{j}(\mathbf{r}_1,\mathbf{r}_2,t)$ in order to explore the synchronicity of the process, i.e., how does the electronic transition $C\,^2\Sigma_u^+ \rightarrow B\,^2\Sigma_u^+$, depicted by the electronic flux density, correlates with the nuclear motion. The electronic
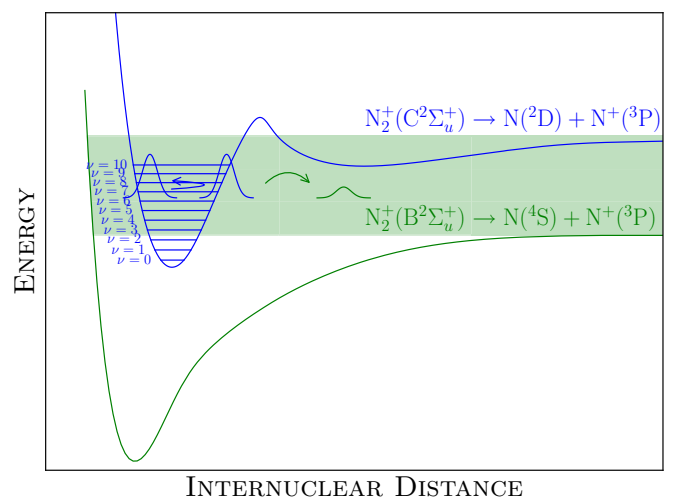
FIG. 1. Representation of the predissociation process. The wave packet in the $C\,^2\Sigma_u^+$ states, created from the ionization of N_2, is continuously transferred into the $B\,^2\Sigma_u^+$ state through the nuclear kinetic energy operator. The green (shadow) box represents the lower part of the continuum of unbound vibrational levels in the $B\,^2\Sigma_u^+$ state.

---

*jperez@zedat.fu-berlin.de; jfperez@udem.edu.co

flux density has been used to study the electronic motion in different scenarios, e.g., coherent electron-nuclear motion in the vibrating H_2^+ molecular ion [12–14] and model systems [15], polarization of the H_2 bond by femtosecond laser pulses [16], $\pi - \pi^*$ transition in ethylene and $n - \pi$ transitions in formaldehyde [17], π electron flux in formic acid dimer on double proton transfer [18], and photoelectron transfer process in alizarin-$(TiO_2)_{15}$ [19]. The paper is organized as follows: In Sec. II we describe the theoretical framework, where the strategy for solving the Schrödinger equation is presented together with the quantum dynamical observables. Section III is devoted for presenting the results and discussions. We first analyze the nuclear dynamics and then the electronic dynamics. We end up in Sec. IV presenting our summary. For completeness, in Appendices A, B, C, and D, we provide a detailed description of the calculation of the nuclear and electronic flux densities, as well as data for the potential energy curves and nonadiabatic couplings.

II. THEORY AND COMPUTATIONS

A. Time-dependent molecular wave function and observables

We express the time-dependent wave function $\Phi(\mathbf{x}; R, t)$ for the aligned molecule as a sum of Born-Oppenheimer vibronic molecular states:

$$\Phi(\mathbf{x}; R, t) = \sum_{\nu_C} c_{\nu_C}(t) \Psi_C(\mathbf{x}; R) \chi_{\nu_C}(R) e^{-i W_{\nu_C} t/\hbar}$$
$$+ \sum_{\nu_B} c_{\nu_B}(t) \Psi_B(\mathbf{x}; R) \chi_{\nu_B}(R) e^{-i W_{\nu_B} t/\hbar}$$
$$+ \int dE c_B(E, t) \Psi_B(\mathbf{x}; R) \chi_B(R, E) e^{-i E t/\hbar}, \quad (1)$$

where $\Psi_C(\mathbf{x}; R)$ and $\Psi_B(\mathbf{x}; R)$ are, respectively, the electronic wave functions for the $C\,^2\Sigma_u^+$ and $B\,^2\Sigma_u^+$ molecular states of the N_2^+ molecular ion, $\mathbf{x}$ labels the spatial and spin coordinates for all electrons, R is the internuclear distance, $\chi_{\nu_C}(R)$ represents a vibrational nuclear wave function of the $C\,^2\Sigma_u^+$ state, $\chi_{\nu_B}(R)$ and $\chi_B(R, E)$ represent a vibrational and a dissociative (continuum) nuclear wave function, respectively, of the $B\,^2\Sigma_u^+$ state, W_{ν_C} and W_{ν_B} are the corresponding energies of the $C\,^2\Sigma_u^+$ and $B\,^2\Sigma_u^+$ vibrational states, and E is the energy of the $B\,^2\Sigma_u^+$ continuum state. In practice, the continuum is discretized through the use of $\mathcal{L}^2$ integrable B-spline basis set [20,21]. Thus Eq. (1) can be recast as

$$\Phi(\mathbf{x}; R, t) = \sum_n \sum_{\nu_n} c_{\nu_n}(t) \Psi_n(\mathbf{x}; R) \chi_{\nu_n}(R) e^{-i W_{\nu_n} t/\hbar}, \quad (2)$$

where n labels the $C\,^2\Sigma_u^+$ and $B\,^2\Sigma_u^+$ molecular states, respectively. The electronic wave functions $\Psi_C(\mathbf{x}; R)$ and $\Psi_B(\mathbf{x}; R)$ are obtained by solving the electronic Schrödinger equation:

$$\mathcal{H}_{el} \Psi_n(\mathbf{x}; R) = E_n(R) \Psi_n(\mathbf{x}; R), \quad (3)$$

where the electronic Hamiltonian $\mathcal{H}_{el}$ is given by

$$\mathcal{H}_{el} = - \sum_i \left(\frac{\hbar^2}{2 m_e} \nabla_{\mathbf{r}_i}^2 + \frac{Z_A e^2}{4 \pi \varepsilon_0 R_{Ai}} + \frac{Z_B e^2}{4 \pi \varepsilon_0 R_{Bi}} \right)$$
$$+ \sum_{i<j} \frac{e^2}{4 \pi \varepsilon_0 r_{ij}} + \frac{Z_A Z_B e^2}{4 \pi \varepsilon_0 R} \quad (4)$$

with $R_{Ai} = |\mathbf{R}_A - \mathbf{r}_i|$ being the distance between electron i and nucleus A (likewise for R_{Bi}) and $r_{ij} = |\mathbf{r}_i - \mathbf{r}_j|$ being the distance between electron i and electron j. The nuclear wave functions $\chi_{\nu_C}(R)$ and $\chi_{\nu_B}(R)$, and the corresponding vibronic energies W_{ν_C} and W_{ν_B}, are then obtained by solving the nuclear Schrödinger equation:

$$\mathcal{H}_{nu} \chi_{\nu_n}(R) = W_{\nu_n} \chi_{\nu_n}(R), \quad (5)$$

where the nuclear Hamiltonian $\mathcal{H}_{nu}$ is given by

$$\mathcal{H}_{nu} = - \frac{\hbar^2}{2M} \frac{\partial^2}{\partial R^2} + E_n(R), \quad (6)$$

where M is the reduced mass of the nuclei. The wave function (2) is then plugged into the Schrödinger equation:

$$i\hbar \frac{\partial}{\partial t} \Phi(\mathbf{x}; R, t) = \mathcal{H} \Phi(\mathbf{x}; R, t) \quad (7)$$

with $\mathcal{H} = \mathcal{H}_{nu} + \mathcal{H}_{el}$ the total Hamiltonian. By projecting onto the basis of stationary vibronic states $\Psi_m(\mathbf{x}, R) \chi_{\mu_m}(R) e^{i W_{\mu_m} t/\hbar}$, we obtain the following set of coupled linear differential equations:

$$\frac{d}{dt} c_{\mu_m}(t) = - \frac{i}{\hbar} \sum_n \sum_{\nu_n} H_{\mu_m, \nu_n} e^{i(W_{\mu_m} - W_{\nu_n}) t/\hbar} c_{\nu_n}(t) \quad (8)$$

with

$$H_{\nu_m, \nu_n} = - \frac{\hbar^2}{2M} \int dR \chi_{\nu_m}(R) \left[2 T_{mn}^{(1)}(R) \frac{\partial}{\partial R} + T_{mn}^{(2)}(R) \right] \chi_{\nu_n}(R), \quad (9)$$

$$T_{mn}^{(1)}(R) = \int d\mathbf{x} \Psi_m(\mathbf{x}; R) \frac{\partial}{\partial R} \Psi_n(\mathbf{x}; R), \quad (10)$$

$$T_{mn}^{(2)}(R) = \int d\mathbf{x} \Psi_m(\mathbf{x}; R) \frac{\partial^2}{\partial R^2} \Psi_n(\mathbf{x}; R). \quad (11)$$

The propagation of Eq. (8) yields the coefficients $c_{\nu_n}(t)$. We assume a Franck-Condon process for the ionization of the $N_2(X\,^1\Sigma_g^+)$. Thus, the initial condition for the expansion coefficients $c_{\nu_C}(0)$, reduces to the projection of the nuclear wave function of the vibrational ground state of $N_2(X\,^1\Sigma_g^+)$ onto the vibrational wave functions $\chi_{\nu_C}(R)$:

$$c_{\nu_C}(0) = \int dR \xi_{N_2(X\,^1\Sigma_g^+, \nu=0)}(R) \chi_{\nu_C}(R), \quad (12)$$

where $\xi_{N_2(X\,^1\Sigma_g^+, \nu=0)}(R)$ is the nuclear wave function of the vibronic ground state of N_2. The *observables of concern* here are the *predissociation rates* given by Fermi's golden rule derived by Dirac [22]:

$$k_{\nu_C} = \frac{2\pi}{\hbar} \varrho(W_{\nu_B}) |H_{\nu_C, \nu_B}|^2 \delta(W_{\nu_C} - W_{\nu_B}), \quad (13)$$

where $\varrho(W_{\nu_B})$ is the density of states of the nuclear continuum of the $B\,^2\Sigma_g{}^+$ electronic state calculated by the three-point formula

$$\varrho(W_{\nu_B}) = \frac{2}{W_{\nu_B+1} - W_{\nu_B-1}}, \qquad (14)$$

the *nuclear probability density*

$$\rho(R,t) = \int d\mathbf{x}\,\Phi^*(\mathbf{x};R,t)\Phi(\mathbf{x};R,t), \qquad (15)$$

the *nuclear flux density*

$$j(R,t) = \mathrm{Re}\left[\frac{\hbar}{iM}\int d\mathbf{x}\,\Phi^*(\mathbf{x};R,t)\frac{\partial}{\partial R}\Phi(\mathbf{x};R,t)\right], \quad (16)$$

and the *two-electron flux density*

$$\mathbf{j}(\mathbf{r}_1,\mathbf{r}_2,t) = \mathrm{Re}\left[\frac{\hbar}{im_e}\int\cdots\int d\mathbf{x}_3\cdots d\mathbf{x}_N d\omega_1 d\omega_2 dR\right.$$
$$\left. \times\,\Phi^*(\mathbf{x};R,t)(\nabla_1+\nabla_2)\Phi(\mathbf{x};R,t)\right], \qquad (17)$$

where $\int d\omega_1$ and $\int d\omega_2$ represent integration over the spin coordinates of electron 1 and electron 2, respectively. For a detailed discussion of n-electron flux density see Ref. [23] where the multidimensional flux density for multiparticle systems is discussed together with the respective multidimensional continuity equation. The two-electron flux density $\mathbf{j}(\mathbf{r}_1,\mathbf{r}_2,t)$ for each electron can be interpreted as the flux density of the electron in consideration, such as at the position $\mathbf{r}_1$, given that the second electron is at the same time in the position $\mathbf{r}_2$. Such a kind of two-particle conditional probability has been used to study electron correlation by looking at the two-electron probability density; see, for example, Refs. [24–26].

B. Nuclear motion

1. Eigenfunctions of the nuclear Hamiltonian

Equation (5) is solved by expanding the nuclear wave function in the basis of B-spline functions

$$\chi_{\nu_n}(R) = \sum_i b_{i\nu_n} B_i^k(R), \qquad (18)$$

where $B_i^k(R)$ is a B-spline function of order k [21]. By inserting (18) into Eq. (5) and projecting onto the $B_j^k(R)$ function one arrives at the secular equation

$$\sum_i\left[\int dR\,B_j^k(R)\mathcal{H}_{\mathrm{nu}}B_i^k(R) - W_{\nu_n}\int dR\,B_j^k(R)B_i^k(R)\right]b_{i\nu_n}$$
$$= 0, \qquad (19)$$

whose solution yields the coefficients $b_{i\nu_n}$ and the eigenvalues W_{ν_n}. In this work, we have used 2200 B-spline functions of order $k=8$ with a linear knot sequence and a box length of $R_{\max}=80a_0$. B-spline functions have been widely used in atomic and molecular physics [20], and they are suited to the challenging task of computing accurate nuclear wave functions for large internuclear distances ($R \to 500a_0$) [27].

2. Partition of nuclear probability and flux densities

Because of the orthogonality of the electronic wave functions [$\Psi_C(\mathbf{x};R)$ and $\Psi_B(\mathbf{x};R)$], the nuclear probability density (15) and nuclear flux density (16) can be split as

$$\rho(R,t) = \rho_C(R,t) + \rho_B(R,t), \qquad (20)$$

$$j(R,t) = j_C(R,t) + j_B(R,t), \qquad (21)$$

where C and B refer to the nuclear density and flux density of the $C\,^2\Sigma_u{}^+$ and $B\,^2\Sigma_u{}^+$ states, respectively. They are calculated as

$$\rho_n(R,t) = \sum_{\mu_n}\sum_{\nu_n} c_{\mu_n}^*(t)c_{\nu_n}(t)\chi_{\mu_n}^*(R)\chi_{\nu_n}(R)e^{i(W_{\mu_n}-W_{\nu_n})t/\hbar},$$
$$(22)$$

$$j_n(R,t) = \frac{\hbar}{iM}\sum_{\mu_n}\sum_{\nu_n} c_{\mu_n}^*(t)c_{\nu_n}(t)\chi_{\mu_n}^*(R)$$
$$\times\,\frac{d}{dR}\chi_{\nu_n}(R)e^{i(W_{\mu_n}-W_{\nu_n})t/\hbar}. \qquad (23)$$

One can define the vibrational and dissociative nuclear probability densities [$\rho_{B,\mathrm{vib}}(R,t)$ and $\rho_{B,\mathrm{dis}}(R,t)$] and the vibrational and dissociative flux densities [$j_{B,\mathrm{vib}}(R,t)$ and $j_{B,\mathrm{dis}}(R,t)$] for the $B\,^2\Sigma_u{}^+$ state by restricting the coefficients in Eqs. (22) and (23). This split leads to interference terms between vibration and dissociation (see Appendix A), nevertheless such interference has a small effect on the total probability density and even a smaller effect on the total flux density as discussed in Ref. [28].

C. Electronic motion

1. Electronic structure of the $N_2{}^+$

We have performed a CASSCF(9,8) calculation [29] (i.e., nine electrons within an active space of eight orbitals) followed by a MRCI-SD calculation [30,31] as implemented in MOLPRO [32]. The electronic eigenfunctions and electronic eigenvalues of Hamiltonian (4) are calculated on a grid spanning the range $1.6a_0 < R < 80a_0$. In order to describe the dissociation limit properly, we include the following IRREPs: $2\times{}^2\Sigma_u{}^+, 2\times{}^2\Delta_u, 2\times{}^4\Sigma_u{}^+, 2\times{}^4\Delta_u, 1\times{}^6\Sigma_u{}^+$. This leads to 13 electronic states and nine potential energy curves (PECs), the Δ states are doubly degenerate. The assignment of the electronic states is done as follows: The lowest PEC corresponds to the $B\,^2\Sigma_u{}^+$ state since the only states lying below are of different symmetry ($X\,^2\Sigma_g{}^+$ and $A\,^2\Pi_u$). The next three PEC cross each other at different internuclear distances and converge to the same dissociating limit. Here we calculate the expectation value of $\hat{L}_z^2$ as a function of the internuclear distance, from which the Σ state ($\langle\hat{L}_z^2\rangle_R = 0$) is separated from the Δ states ($\langle\hat{L}_z^2\rangle_R = 4$), thus the $C\,^2\Sigma_u{}^+$ state can be chosen accordingly. Our assignment is in good agreement with those reported by Roche and Lefebvre-Brion [33], Langhof et al. [34], Langhoff and Bauschlicher [35], and Liu et al. [36]. We compare results obtained with two basis sets, the aug-cc-pVQZ (AVQZ) and aug-cc-pV5Z (AV5Z) [37]. No significant differences were observed.

2. Nonadiabatic couplings between $C\,^2\Sigma_u^+$ and $B\,^2\Sigma_u^+$ states

The coupling function $T_{BC}^{(1)}(R)$ [Eq. (10)] was calculated for each internuclear distance on the grid $1.6a_0 < R < 80a_0$ by means of the finite difference methodology as implemented in MOLPRO [32]. The numerical derivative was performed by using $\Delta R = 0.01$ Å $= 0.0189a_0$. The second order nonadiabatic coupling function $T_{BC}^{(2)}(R)$ [Eq. (11)] was estimated to be

$$T_{BC}^{(2)}(R) \approx \frac{d}{dR}T_{BC}^{(1)}(R). \tag{24}$$

The quality of the approximation in Eq. (24) was studied by comparing each of the matrix element H_{ν_C,ν_B} with its transpose H_{ν_B,ν_C}. In the ideal case (complete basis set) one has $H_{\nu_C,\nu_B} = H_{\nu_B,\nu_C}$. Here we obtained for the largest difference $|H_{\nu_C,\nu_B} - H_{\nu_B,\nu_C}| = 0.00001\ E_h$. In practice we set $H_{\nu_C,\nu_B} = H_{\nu_B,\nu_C}$ in order to guarantee that $\mathcal{H}$ is Hermitian in the basis of vibronic states employed.

3. The two-electron flux density

The configuration interaction (CI) wave function for the $B\,^2\Sigma_u^+$ and $C\,^2\Sigma_u^+$ states read

$$\Psi_B(\mathbf{x}; R) = \sum_i C_{iB}(R)\psi_i(\mathbf{x}; R) \tag{25}$$

and

$$\Psi_C(\mathbf{x}; R) = \sum_i C_{iC}(R)\psi_i(\mathbf{x}; R), \tag{26}$$

respectively. In Table I the occupation pattern of four configurations ψ_i are listed, together with their weight in the CI expansion at equilibrium distance of the respective electronic state. The first two configurations (ψ_1 and ψ_2) have the largest weights, and thus are the most important ones. Due to the dominant behavior of the $C_{1C}(R)$, $C_{2C}(R)$, $C_{1B}(R)$ and $C_{2B}(R)$ coefficients with respect to the rest of the configuration interaction coefficients, both electronic states can be represented in a good approximation by only these two configurations as discussed in Ref. [6]. Note that ψ_2, ψ_3, and ψ_4 differ only in their spins. Thus we include only ψ_2 in our treatment, even though ψ_2 and ψ_3 have similar weights. For comparison, a treatment including ψ_3 as a third configuration is presented in Appendix C. Further note that each pair of ψ_i and ψ_j differ by two molecular spin orbitals (see Table I). The one-electron flux density arises from pairs of configurations differing by no more than one molecular orbitals [16], thus the one-electron flux density vanishes if only the four ψ_i listed in Table I are considered. Therefore we opted to calculate the two-electron flux density Eq. (17) instead, which can be formally obtained from the time-dependent wave function Eq. (2) as the expectation value of the two-electron flux density operator $\hat{j}(\mathbf{r}_1', \mathbf{r}_2')$ (see Appendix B) as follows:

$$\mathbf{j}(\mathbf{r}_1', \mathbf{r}_2', t) = \mathrm{Re}[\langle \Phi(t)|\hat{j}(\mathbf{r}_1', \mathbf{r}_2')|\Phi(t)\rangle]. \tag{27}$$

Substitution of Eq. (2) into Eq. (27) gives us

$$\mathbf{j}(\mathbf{r}_1', \mathbf{r}_2', t) = \mathbf{j}_B^{\mathrm{AEFD}}(\mathbf{r}_1', \mathbf{r}_2', t) + \mathbf{j}_C^{\mathrm{AEFD}}(\mathbf{r}_1', \mathbf{r}_2', t) + \mathbf{j}_{BC}^{\mathrm{TEFD}}(\mathbf{r}_1', \mathbf{r}_2', t) \tag{28}$$

with

$$\begin{aligned}\mathbf{j}_B^{\mathrm{AEFD}}(\mathbf{r}_1', \mathbf{r}_2', t) = \mathrm{Re}\Bigg[&\int dR \langle \Psi_B(R)|\hat{j}(\mathbf{r}_1', \mathbf{r}_2')|\Psi_B(R)\rangle \\ &\times \sum_{\nu_B \nu_B} c_{\nu_B}^*(t)c_{\nu_B}(t)\chi_{\nu_B}^*(R)\chi_{\nu_B}(R) \\ &\times e^{i(W_{\nu_B}-W_{\nu_B})t/\hbar}\Bigg] = 0, \end{aligned} \tag{29}$$

$$\begin{aligned}\mathbf{j}_C^{\mathrm{AEFD}}(\mathbf{r}_1', \mathbf{r}_2', t) = \mathrm{Re}\Bigg[&\int dR \langle \Psi_C(R)|\hat{j}(\mathbf{r}_1', \mathbf{r}_2')|\Psi_C(R)\rangle \\ &\times \sum_{\nu_C \nu_C} c_{\nu_C}^*(t)c_{\nu_C}(t)\chi_{\nu_C}^*(R)\chi_{\nu_C}(R) \\ &\times e^{i(W_{\nu_C}-W_{\nu_C})t/\hbar}\Bigg] = 0, \end{aligned} \tag{30}$$

and

$$\mathbf{j}_{BC}^{\mathrm{TEFD}}(\mathbf{r}_1', \mathbf{r}_2', t) = i\int dR\,\mathbf{\Lambda}_{BC}(\mathbf{r}_1', \mathbf{r}_2'; R)G_{BC}(R, t), \tag{31}$$

where AEFD stands for adiabatic electronic flux density and TEFD stands for transition electronic flux density. The AEFD vanishes since the two-electron flux density operator $\hat{j}(\mathbf{r}_1', \mathbf{r}_2')$ is imaginary. This is a failure of the Born-Oppenheimer separation in Eq. (1) and is discussed in Refs. [38–40]. The AEFD is driven only by the nuclear motion in a single potential energy curve $E_n(R)$ playing no role in the predissociation process. Besides its vanishing behavior in the Born-Oppenheimer approximation, it can be estimated to be equal to the electronic density associated to each nucleus (by means of using projection operators) multiplied by the relative velocity between the two nuclei [16]. Here we deal only with the TEFD, which arises from the coherent superposition between the $C\,^2\Sigma_u^+$ and $B\,^2\Sigma_u^+$ states, where the nuclear motion plays a secondary role. The TEFD in Eq. (31) depends functionally on the R-dependent vector field

$$\begin{aligned}\mathbf{\Lambda}_{BC}(\mathbf{r}_1', \mathbf{r}_2'; R) &= \langle \Psi_B(R)|\hat{j}(\mathbf{r}_1', \mathbf{r}_2')|\Psi_C(R)\rangle \\ &\quad - \langle \Psi_C(R)|\hat{j}(\mathbf{r}_1', \mathbf{r}_2')|\Psi_B(R)\rangle \end{aligned} \tag{32}$$

TABLE I. Occupation pattern of the four configurations ψ_1, ψ_2, ψ_3, and ψ_4 and their weights $|C_{iC}|^2$ and $|C_{iB}|^2$ in the CI expansion at equilibrium distance. In first approximation, only ψ_1 and ψ_2 are needed to describe the predissociation process $C\,^2\Sigma_u^+ \to B\,^2\Sigma_u^+$ of N_2^+ [6]. Only molecular orbitals $3\sigma_g$, $2\sigma_u$, $1\pi_u$, and $1\pi_g$ are needed to calculate the two-electron flux density.

	$2\sigma_g$	$3\sigma_g$	$1\pi_u$	$1\pi_u$	$2\sigma_u$	$3\sigma_u$	$1\pi_g$	$1\pi_g$	$|C_{iC}|^2$	$|C_{iB}|^2$
ψ_1	$\uparrow\downarrow$	$\uparrow\downarrow$	$\uparrow\downarrow$	$\uparrow\downarrow$	$\uparrow$	0	0	0	0.202	0.769
ψ_2	$\uparrow\downarrow$	$\uparrow$	$\downarrow$	$\uparrow\downarrow$	$\uparrow\downarrow$	0	$\uparrow$	0	0.178	0.051
ψ_3	$\uparrow\downarrow$	$\uparrow$	$\uparrow$	$\uparrow\downarrow$	$\uparrow\downarrow$	0	$\downarrow$	0	0.146	0.003
ψ_4	$\uparrow\downarrow$	$\downarrow$	$\uparrow$	$\uparrow\downarrow$	$\uparrow\downarrow$	0	$\uparrow$	0	≈ 0	≈ 0

TABLE II. Energies W_{v_C}, initial amplitudes $c_{v_C}(0)$, and predissociation rates k_{v_C} of the bound vibrational states v_C. The energies W_{v_B} of the discretized continuum states v_B are also listed.

v_C	$W_{v_C}(E_h)$	v_B	$W_{v_B}(E_h)$	$c_{v_C}(0)$	$k_{v_C}(10^8 \text{ s}^{-1})$
0	$-108.533\,532$	–	–	$0.057\,799$	–
1	$-108.524\,214$	–	–	$-0.127\,575$	–
2	$-108.514\,974$	–	–	$0.204\,161$	–
3	$-108.505\,869$	180	$-108.505\,895$	$0.272\,566$	1.39
4	$-108.496\,891$	433	$-108.496\,941$	$-0.323\,173$	4.06
5	$-108.488\,031$	577	$-108.488\,091$	$0.352\,044$	6.18
6	$-108.479\,290$	689	$-108.479\,351$	$0.358\,046$	9.29
7	$-108.470\,727$	783	$-108.470\,771$	$-0.345\,065$	13.58
8	$-108.462\,334$	865	$-108.462\,362$	$0.320\,044$	19.47
9	$-108.454\,094$	938	$-108.454\,164$	$0.286\,741$	27.43
10	$-108.446\,039$	1005	$-108.446\,021$	$-0.250\,082$	36.40

and on the time and R-dependent scalar function

$$G_{BC}(R,t) = \text{Re}\left[\sum_{v_B v_C} c_{v_B}^*(t) c_{v_C}(t) \chi_{v_B}^*(R) \chi_{v_C}(R) \right.$$

$$\left. \times\, e^{i(W_{v_B}-W_{v_C})t/\hbar} \right]. \quad (33)$$

Notice that integration over R in Eq. (31) gives rise to the correlation between electrons and nuclei, thus describing the nonadiabatic dynamics of the predissociation process.

III. RESULTS AND DISCUSSION

A. Nuclear dynamics

First, we present the predissociation rates k_{v_C} as obtained from Fermi's golden rule [Eq. (13)]. They are listed in Table II, together with the energies (W_{v_C} and W_{v_B}) and vibrational quantum numbers (v_C and v_B) of the involved states. Note that the B-spline box is large enough ($80 a_0$) to provide a dense energy spectrum of the nuclear continuum of the $B\,{}^2\Sigma_u^+$ state such that the delta condition $\delta(W_{v_C} - W_{v_B})$ is fulfilled (compare W_{v_C} with W_{v_B}). The coefficients $c_{v_C}(0)$ corresponding to the Franck-Condon factors between the vibrational ground state of N_2 and the vibrational wave functions $\chi_{v_C}(R)$ are also listed. Figure 2 shows our calculated predissociation rates (from $v_C = 3$ to $v_C = 30$) and compares with the experimental results reported in Ref. [6] (from $v_C = 3$ to $v_C = 9$). Note that the predissociation rates of some vibrational states v_C do not appear in Fig. 2, because the respective vibrational wave functions $\chi_{v_C}(R)$ are localized in the outer part of the double well potential $E_C(R)$ (see Fig. 1), yielding predissociation rates too small ($k_{v_C} < 10^8 \text{ s}^{-1}$).

From the time evolution of the population of the continuum $B\,{}^2\Sigma_u^+$, i.e., $p_{\text{dis}}(t)$, one can estimate the predissociation rate k_p of the vibrational wave packet of the $C\,{}^2\Sigma_u^+$ state by

$$k_p = \frac{d}{dt} p_{\text{dis}}(t) \approx \frac{\Delta p_{\text{dis}}}{\Delta t}, \quad (34)$$

which gives us in average (see Fig. 3) $0.00085/600\,\text{fs} = 14.17 \times 10^8\,\text{s}^{-1}$. This result agrees well with the predissociation
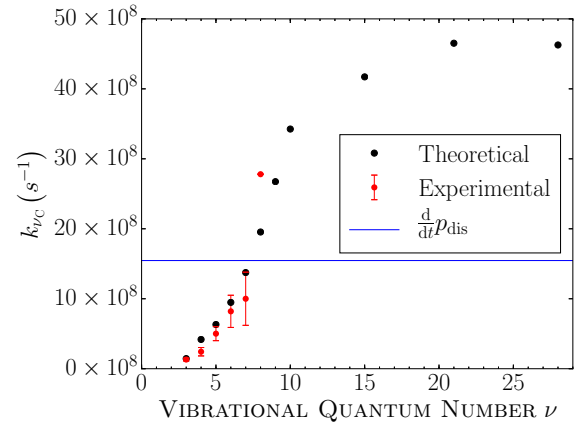
FIG. 2. Calculated (black dots) and experimental (red dots with error bars) predissociation rates k_{v_C}. The mean value of the predissociation rate of the vibrational wave packet of the $C\,{}^2\Sigma_u^+$ state is indicated with a horizontal line.

rates of the dominant (most populated) $v_C = 4$, $v_C = 5$, $v_C = 6$, $v_C = 7$, and $v_C = 8$ vibrational states (see Table II).

Next let us present the first 600 fs of the dynamics. We consider the nuclear probability densities $\rho_C(R,t)$, $\rho_{B,\text{vib}}(R,t)$, and $\rho_{B,\text{dis}}(R,t)$, with the corresponding populations $p_C(t) = \int dR \rho_C(R,t)$, $p_{B,\text{vib}}(t) = \int dR \rho_{B,\text{vib}}(R,t)$, and $p_{B,\text{dis}}(t) = \int dR \rho_{B,\text{dis}}(R,t)$, respectively. Figure 3 displays the nuclear probability densities as a function of the time and as a function of the internuclear distance (lower panels) together with the corresponding populations (upper panels). During the first 100 fs, the nuclear probability density $\rho_C(R,t)$ reveals a quasiperiodic pattern with structure, corresponding to alternating bond stretches and compressions with classical period of about 18.2 fs. Note that during the first vibration, the population of the $C\,{}^2\Sigma_u^+$ state decreases from 0.955 to 0.953 in the first 4.5 fs, followed by a build up to 0.955 from 4.4 to 9.1 fs. This depletion-build up process is then repeated during the second half of the vibration completing the first bond stretching-bond compression in 18.2 fs. The next 60 fs is then characterized by three vibrations, the bond stretching-bond compression cycle is then repeated successively leading the dephasing of the nuclear wave packet together with a decrease of $p_C(t)$ to 0.954 at 80 fs. The total population $p(t) = p_C(t) + p_{B,\text{vib}}(t) + p_{B,\text{dis}}(t)$ must be conserved during the entire dynamics. We have checked that at any time $p(t)$ is constant within 10^{-7} of uncertainty. Thus the oscillatory behavior of $p_C(t)$ should be reflected in the population of the $B\,{}^2\Sigma_u^+$ state. Note that during the first vibration $p_{B,\text{vib}}(t)$ experiences twice a build up-depletion process, which correlates well with the oscillations observed in $p_C(t)$. In contrast, $p_{B,\text{dis}}(t)$ builds up abruptly around 4 fs followed by a depletion and then builds up again around 13 fs with the subsequent depletion, thus during the first vibration $p_{B,\text{dis}}(t)$ experiences two build ups, the first one coinciding with the bond stretching and the second one with the bond compression. During the next three vibrations $p_{B,\text{vib}}(t)$ and $p_{B,\text{dis}}(t)$ behave in a similar manner as during the first vibration but this time accompanied by the dephasing of the wave packets (see Fig. 3). Thus, during the first 100 fs, the
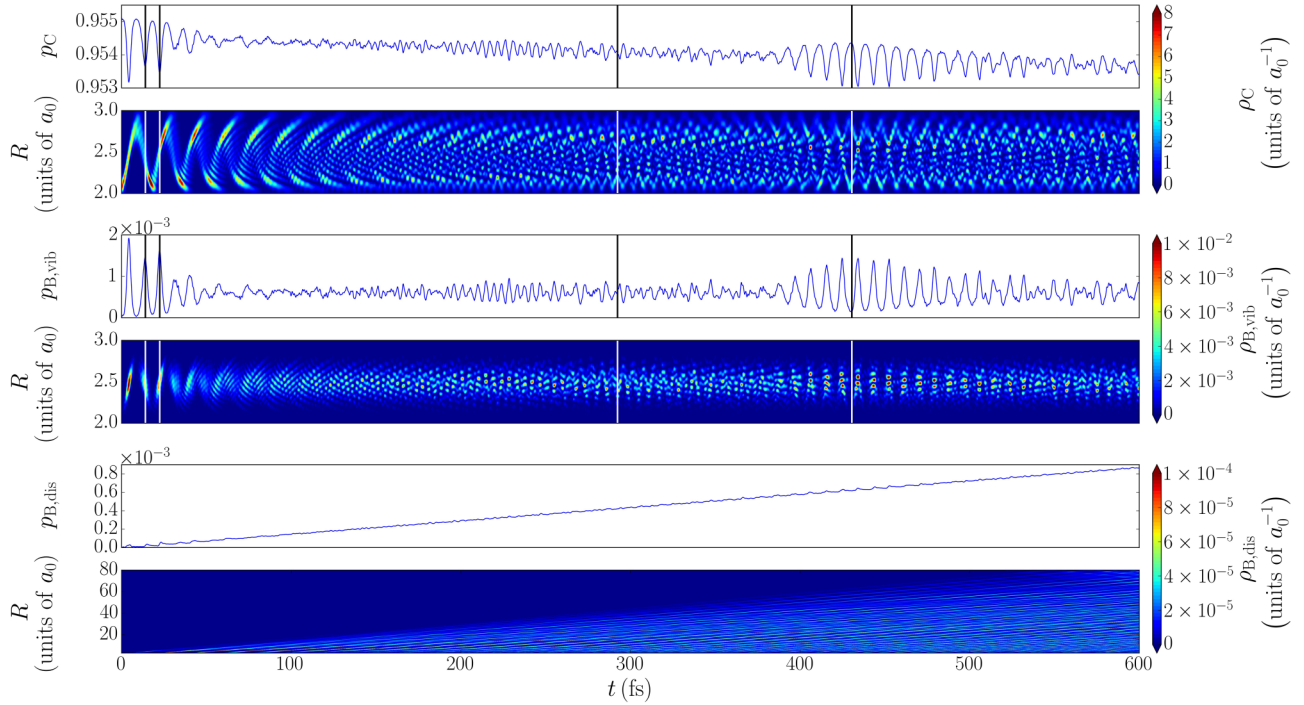
FIG. 3. From top to the bottom: probability densities $\rho_C(R,t)$, $\rho_{B,\mathrm{vib}}(R,t)$, and $\rho_{B,\mathrm{dis}}(R,t)$ in units of a_0^{-1}, together with their corresponding populations. The internuclear distance R is in units of a_0. In the lower two panels the $B\,{}^2\Sigma_u^+$ state was split into a vibrating and a dissociative part by only including bound and unbound vibrational states, respectively [see Eqs. (A3) and (A4)].

probability of finding the system in the continuum does not grow linearly in time, i.e., Fermi's golden rule breaks down. From 100 until 400 fs the dynamics is irregular, i.e., the wave packets $\rho_C(R,t)$ and $\rho_{B,\mathrm{vib}}(R,t)$ experience the dephasing being $\rho_C(R,t)$ delocalized from $R = 2.0a_0$ to $R = 3.0a_0$ while $\rho_{B,\mathrm{vib}}(R,t)$ covers only a small region from $R = 2.3a_0$ to $R = 2.6a_0$. In contrast, $\rho_{B,\mathrm{dis}}(R,t)$ seems to cover large internuclear distances assembling a train of wave packets. During this period, from 100 to 400 fs, the population of the vibrating part of the $B\,{}^2\Sigma_u^+$ state oscillates around a constant value (~ 0.0005), while the population of the $C\,{}^2\Sigma_u^+$ state oscillates at the same time that its average decreases linearly according to $\bar{p}_C(t) = p_C(0) - k_p t$. The linear depletion in the population of the $C\,{}^2\Sigma_u^+$ state is better visible by the linear grow of the population of the dissociating part of the $B\,{}^2\Sigma_u^+$ state, i.e., the dynamics is now governed by Fermi's golden rule according to $p_{B,\mathrm{dis}}(t) = k_p t$. At about 400 fs the populations of the vibrating $C\,{}^2\Sigma_u^+$ and $B\,{}^2\Sigma_u^+$ states suggest that the revival time (or at least a fractional revival time [41]) has been reached. Note that from 400 until 500 fs the populations of the vibrating $C\,{}^2\Sigma_u^+$ and $B\,{}^2\Sigma_u^+$ states oscillates with a period of about 20 fs. However, the nuclear probability densities $\rho_C(R,t)$ and $\rho_{B,\mathrm{vib}}(R,t)$ do not exhibit their initial compact form. Instead of that, from 400 until 500 fs we notice that the nuclear wave packet $C\,{}^2\Sigma_u^+$ is split into two wave packets, while $\rho_{B,\mathrm{vib}}(R,t)$ exhibits a strong interfering pattern. This effect in the $C\,{}^2\Sigma_u^+$ state is analogous to the wave packet interferometry observed in the vibrating I_2 molecule [42], where the two wave packets are coherently created by two laser pulses with a specific time delay. Here the $B\,{}^2\Sigma_u^+$ state acts like a filter which split the nuclear wave packet in the $C\,{}^2\Sigma_u^+$ state. This dephasing and revival of nuclear wave

packets has been experimentally observed in the H_2^+ (D_2^+) molecular ion [10,43,44] and in the Br_2 molecule [45]. After 500 fs the dynamics starts again with the dephasing of the wave packets. Figure 4 displays the nuclear flux densities (from 0 until 600 fs) $j_C(R,t)$, $j_{B,\mathrm{vib}}(R,t)$, and $j_{B,\mathrm{dis}}(R,t)$ together with their respective integrals $v_C(t) = \int dR j_C(R,t)$, $v_{B,\mathrm{vib}}(t) = \int dR j_{B,\mathrm{vib}}(R,t)$, and $v_{B,\mathrm{dis}}(t) = \int dR j_{B,\mathrm{vib}}(R,t)$. In general, the flux densities are similar to the probability densities, i.e., they exhibit the vibrational motion in the $C\,{}^2\Sigma_u^+$ and $B\,{}^2\Sigma_u^+$ states with strong oscillations during the first 100 fs, and subsequent dephasing (vanishing flux density) until 400 fs when the revival is reached (strong flux density). The dissociation throughout the continuum $B\,{}^2\Sigma_u^+$ state is also observed. Surprisingly, the integrated fluxes $v(t)$ exhibit a different oscillatory behavior when compared with the populations $p(t)$ (integrated probability densities); for example, $v_C(t)$ does not display a chaotic behavior from 100 to 400 fs; instead of that, the frequency of the oscillation keeps constant and only the amplitude of $v_C(t)$ is affected. From 400 to 500 fs (assembling of the wave packet) the amplitude in $v_C(t)$ is not enhanced significantly but its frequency seems to be doubled. The dynamics for the vibrating $B\,{}^2\Sigma_u^+$ state is different; for example, besides the chaotic behavior observed after 100 fs, the revival at 400 fs is barely observed (see Fig. 4 from 400 to 500 fs center panel). More interesting is the behavior of $v_{B,\mathrm{vib}}(t)$ from ~ 260 to ~ 320 fs where the flux recovers its regular oscillatory pattern and the frequency seems to be doubled. At this point of the discussion we remark that the total probability density $\rho(R,t)$ and the total flux density $j(R,t)$ fulfills the continuity equation, i.e., $\partial_t \rho(R,t) + \partial_R j(R,t) = 0$, as a consequence of the conservation of the probability [46]; however, since there is
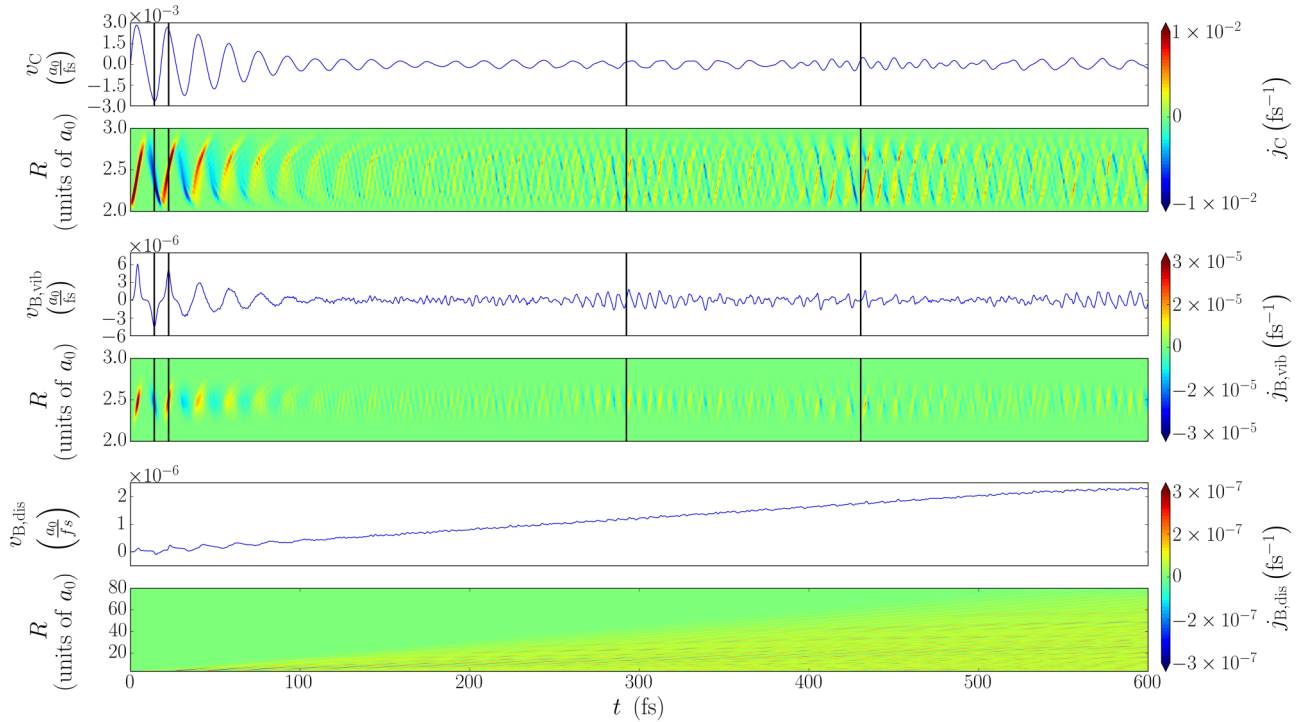
FIG. 4. Nuclear flux densities. From top to the bottom: $j_C(R,t)$, $j_{B,\text{vib}}(R,t)$, and $j_{B,\text{dis}}(R,t)$ in units of fs^{-1}. The internuclear distance R is in units of a_0, and the integrated fluxes v_n are in units of a_0/fs. In the lower two panels the $B\,^2\Sigma_u^+$ state was split into a vibrating and a dissociative just as for the densities in Fig. 3 [see also Eqs. (A7) and (A8)].

a transfer of population from one electronic state to the other, we cannot expect the continuity equation to be fulfilled for each pair of probability and flux densities (ρ_n, j_n) with $n = C, B$. Thus, a pattern observed either in $\rho_C(R,t)$ or $\rho_B(R,t)$ can be "mapped" to $j_C(R,t)$ and $j_B(R,t)$ in many different ways. Figure 5 displays snapshots of $\rho_C(R,t)$ and $j_C(R,t)$ embedded in the potential energy curve $E_C(R)$, and $\rho_B(R,t)$ and $j_B(R,t)$ embedded in the potential energy curve $E_B(R)$ at the specific times 13.98, 22.41, 292.37, and 430.54 fs, which are indicated by vertical lines in Figs. 3 and 4. At 13.98 fs, we found synchronous C and B wave packets for the bond compression (negative flux density); i.e., the wave packet in the C state is basically mapped into the $E_B(R)$ potential energy curve, and both probability and flux densities look similar. At 22.41 fs, the nuclear motion is still coherent in both potential energy

curves $E_C(R)$ and $E_B(R)$, in the sense that the probability density and flux density still look quite similar, but for bond stretching this time (positive flux density). At 292.37 fs, we still find some coherences; for example, both wave packets are characterized by bond stretching (at short internuclear distance) and bond compression (at large internuclear distance). However, the dephasing of the wave packets appears quite different [compare $\rho_C(R,t)$ and $\rho_B(R,t)$]. At 430.54 fs, the nuclear distributions in the $C\,^2\Sigma_u^+$ and $B\,^2\Sigma_u^+$ states are rather different; we recognize a quasivanishing $\rho_B(R,t)$ localized at $R = 2.4a_0$, while $\rho_C(R,t)$ and $j_C(R,t)$ reveal a split of the nuclear distribution localized at the inner and outer classical turning points. In fact, the nuclear flux density of the $C\,^2\Sigma_u^+$ state reveals two wave packets traveling in opposite directions.
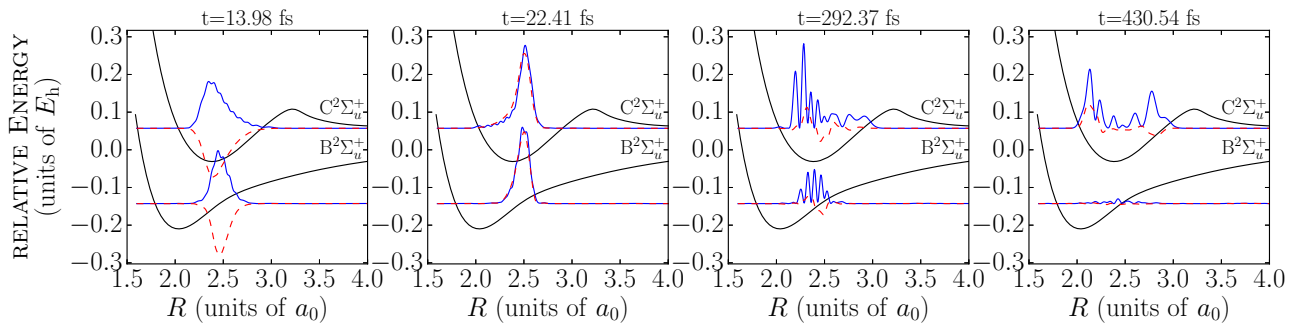
FIG. 5. Snapshots of the wave packets as nuclear probabilities $\rho_C(R,t)$ and $\rho_B(R,t)$ (blue solid lines) and flux densities $j_C(R,t)$ and $j_C(R,t)$ (red dashed lines) in their respective potential wells. The four selected time steps are indicated as vertical lines in Figs. 3 and 4 as well. The energy is given relative to the dissociation limit of the $B\,^2\Sigma_u^+$ state.
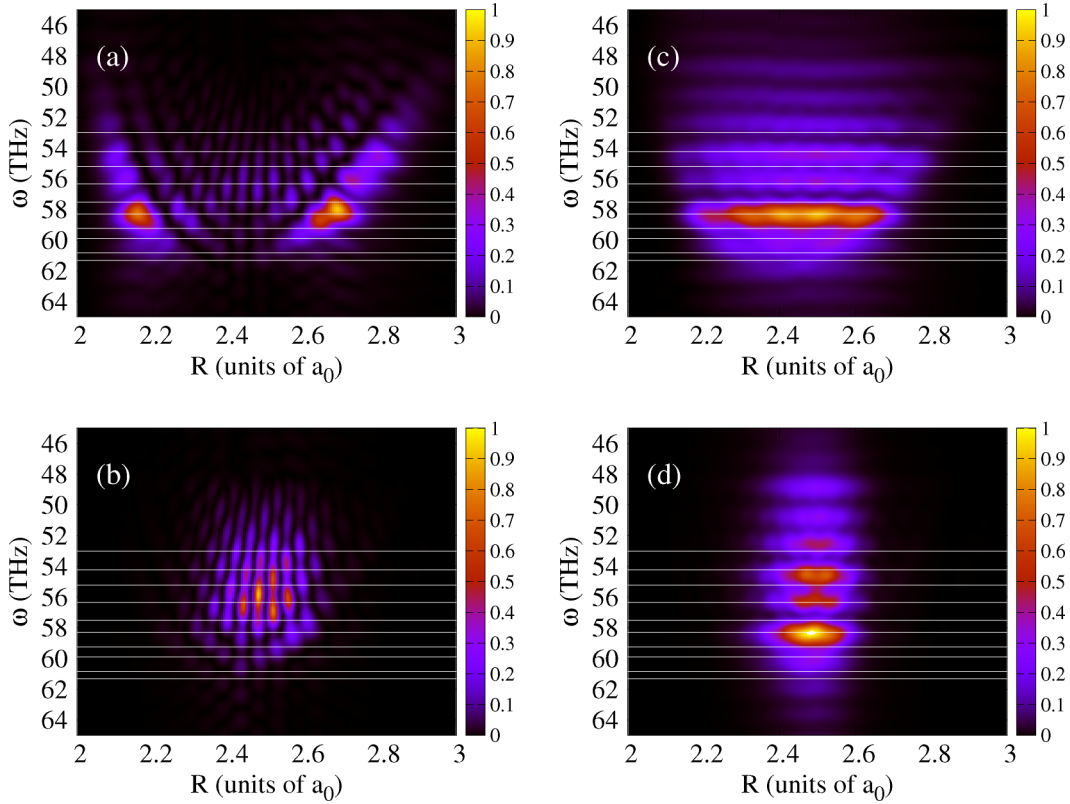
FIG. 6. Power spectra of the N_2^+ molecular ion. Power spectrum of (a) the nuclear probability density $|\tilde{\rho}_C(R,\omega; T = 600\,\text{fs})|^2$, (b) the nuclear probability density $|\tilde{\rho}_B(R,\omega; T = 600\,\text{fs})|^2$, (c) the nuclear flux density $|\tilde{j}_C(R,\omega; T = 600\,\text{fs})|^2$, and (d) the nuclear flux density $|\tilde{j}_B(R,\omega; T = 600\,\text{fs})|^2$. The horizontal white lines indicate the quantum beat series $W_{\nu_c+1} - W_{\nu_c}$ for $\nu_c = 1 - 10$.

1. Fourier analysis of the nuclear probability and flux densities

The nuclear probability density and nuclear flux density Eqs. (22) and (23) contain information about the nuclear dynamics not only in the time-space domain, but also in the frequency-space domain [44,47–49]. Thus Fourier analysis or power spectra (also known as quantum-beat spectra) of $\rho_n(R,t)$ and $j_n(R,t)$,

$$|\tilde{\rho}_n(R,\omega; T)|^2 = \left| \frac{1}{\sqrt{2\pi}} \int_0^T \rho_n(R,t) e^{-i\omega t}\, dt \right|^2, \quad (35)$$

$$|\tilde{j}_n(R,\omega; T)|^2 = \left| \frac{1}{\sqrt{2\pi}} \int_0^T j_n(R,t) e^{-i\omega t}\, dt \right|^2, \quad (36)$$

provide in principle the nodal structure and the inflection points of the nuclear wave functions $\chi_{\nu_n}(R)$ [49], from which one can imaging the potential energy curve $E_n(R)$. Because of nonadiabatic couplings between the electronic states $C\,^2\Sigma_u^+$ and $B\,^2\Sigma_u^+$, the nuclear wave packets characterized by $[\rho_C(R,t),\, j_C(R,t)]$ and $[\rho_B(R,t),\, j_B(R,t)]$ do not evolve freely in their potential energy curves $E_n(R)$. Thus, Fourier transforms $[|\tilde{\rho}_C(R,\omega,T)|^2, |\tilde{j}_C(R,\omega,T)|^2]$ and $[|\tilde{\rho}_B(R,\omega,T)|^2, |\tilde{j}_B(R,\omega,T)|^2]$ might deviate considerably from the adiabatic case [49]. Figure 6 shows the power spectra $|\tilde{\rho}_C(R,\omega; T)|^2$, $|\tilde{\rho}_B(R,\omega; T)|^2$, $|\tilde{j}_C(R,\omega; T)|^2$, and $|\tilde{j}_B(R,\omega; T)|^2$ for a time sampling of $T = 600$ fs. The quantum beats frequencies $(\nu_C, \nu_C + 1)$ are displayed as horizontal lines. In general, the

quantum beat $(4,5)$ exhibits the strongest signal. The power spectra of the $C\,^2\Sigma_u^+$ state looks similar to the power spectra of an adiabatic propagation of a wave packet, i.e., the probability density depicts the boundaries of the potential $E_C(R)$ with the nodal structure of the nuclear wave functions $\chi_{\nu_C}(R)$ and $\chi_{\nu_C+1}(R)$ in between, while the flux density displays no nodes but several maxima and minima instead, depicting the inflection points of the $\chi_{\nu_C}(R)$ functions [49]. This is due to the fact that at 600 fs the $C\,^2\Sigma_g^+$ has lost only 0.2% of its original population, thus the nonadiabatic coupling barely perturbs the free propagation of the nuclear wave packet. In contrast, the propagation of the nuclear wave packet in the $B\,^2\Sigma_u^+$ state is not adiabatic at all, i.e., all its population which saturates to ~ 0.0005 after the first 100 fs of the dynamics oscillates considerably until 600 fs. Thus, the power spectra of $\rho_B(R,t)$ and $j_B(R,t)$ deviate considerably from the expected behavior; e.g., the boundaries of the potential $E_B(R)$ are not revealed. This is not only due to the time variation of the population of the $B\,^2\Sigma_u^+$ state but also to the fact that the maximum population in the $B\,^2\Sigma_u^+$ state is reached precisely when the probability density is located around $R \sim 2.5a_0$ with no contribution on the boundaries of the $E_B(R)$ potential, and being minimum when $\rho_B(R,t)$ is reflected by either the inner or the outer turning point. In other words, the $\rho_B(R,t)$ [and thereof $j_B(R,t)$] does not scan completely the $E_B(R)$ potential. Surprisingly, the quantum beat $(4,5)$ can be identified in $|\tilde{j}_B(R,\omega; T)|^2$ but not in $|\tilde{\rho}_B(R,\omega; T)|^2$.
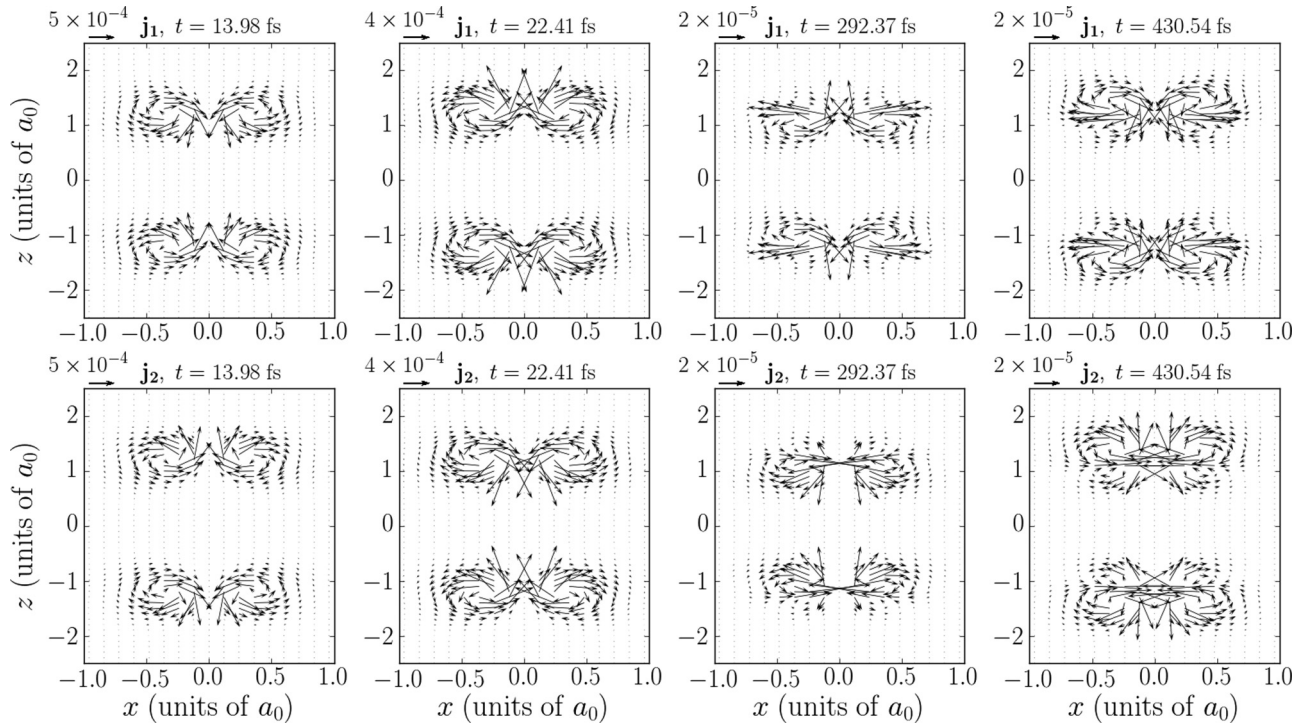
FIG. 7. Snapshots of the two-electron flux density $\mathbf{j}_{BC}^{\text{TEFD}}(\mathbf{r}_1',\mathbf{r}_2',t) = (\mathbf{j}_1(\mathbf{r}_1,\mathbf{r}_2,t),\mathbf{j}_2(\mathbf{r}_1,\mathbf{r}_2,t))$ with $\mathbf{r}_1 = (x, y = 0, z)$ and $\mathbf{r}_2 = -\mathbf{r}_1$ at the four characteristic times: $t = 13.98$ fs, $t = 22.41$ fs, $t = 292.37$ fs, and $t = 430.54$ fs. The vector field was calculated as follows: $\mathbf{j}_{BC}^{\text{TEFD}}(\mathbf{r}_1,\mathbf{r}_2,t) = i \int dR \boldsymbol{\Lambda}_{BC}(\mathbf{r}_1,\mathbf{r}_2; R) G_{BC}(R,t)$ with $\boldsymbol{\Lambda}_{BC}(\mathbf{r}_1,\mathbf{r}_2; R) = \boldsymbol{\lambda}_{BC}^{12}(\mathbf{r}_1,\mathbf{r}_2; R)$ (see Appendix B).

B. Electron dynamics

In this section we turn our attention to the electronic motion. During the predissociation process, the electronic wave function can be represented as a linear combination of the the $C\,^2\Sigma_u{}^+$ and the $B\,^2\Sigma_u{}^+$ states. Thus a coherent electronic wave packet results from the superposition of both electronic states and therefore an electronic flux density is expected. The mentioned electronic flux density, also called transition electronic flux density, has a different nature as the adiabatic electronic flux density. The latter is due to the nuclear motion, i.e., the electrons follow the nuclei. In the H_2 molecule it has been shown that the transition electronic flux density can be up to three orders of magnitude larger than the adiabatic, thus we focus on the transition flux density here. As appears in Eq. (31), there is a nuclear $G_{BC}(R,t)$ and an electronic $\boldsymbol{\Lambda}_{BC}(\mathbf{r}_1',\mathbf{r}_2'; R)$ contribution to the TEFD. From the latter one the shape of the flux densities arises. The former one includes the interference between the two nuclear wave functions $\chi_C(R,t)$ and $\chi_B(R,t)$ and can be regarded as a weight function when integrating over R, thus determining when and where an electron flux density does appear. Additionally, it carries the time dependence of the nuclear motion. Note that the two-electron TEFD is a vector field of dimension 6 for a fixed time t. In order to visualize the two-electron flux density we set $\mathbf{r}_2 = -\mathbf{r}_1$, and then we plot the separated components $\mathbf{j}_1(\mathbf{r}_1,\mathbf{r}_2,t)$ and $\mathbf{j}_2(\mathbf{r}_1,\mathbf{r}_2,t)$ in the xz plane, i.e., the cylindrical symmetry of the molecule is exploited. Figure 7 displays the two-electron flux density $\mathbf{j} = (\mathbf{j}_1,\mathbf{j}_2)$ taking into account only two configurations (ψ_1 and ψ_2) of the CI expansion. By including the configuration ψ_3, the shape of the vector field does not change, only its magnitude is affected (see Appendix C for an explicit discussion). In

general, the electronic flux density depicts a π-like current, i.e., the flux density vanishes along the molecular axis (z axis, $x = 0$) and localizes at the lobes characteristic of a π-molecular orbital; see Fig. 8 where the molecular orbitals involved in the TEFD are shown. Thus, one can recognize four lobes in the TEFD, each one with the characteristics of a rotating vector field. It is important to notice that there is not a net electronic flux from one atomic center to the other (the vector field preserves the ungerade symmetry of the electronic wave function). Also one can see that the lobes of $\mathbf{j}_1$ rotate in opposite directions of the lobes of $\mathbf{j}_2$. We find that the z-component of $\mathbf{j}_1$ for $x \to 0$ always points in the direction of the nuclear motion; for example, at 13.98 fs we found a compression of the bound, and at $t = 22.41$ fs a stretching of the bound, i.e., the z component of $\mathbf{j}_1$ is synchronized with the nuclear motion. At $t = 292.37$ and $t = 430.54$ fs the z component of $\mathbf{j}_1$ suggests the motion of two nuclear wave packets in opposite directions (compare with Fig. 5);
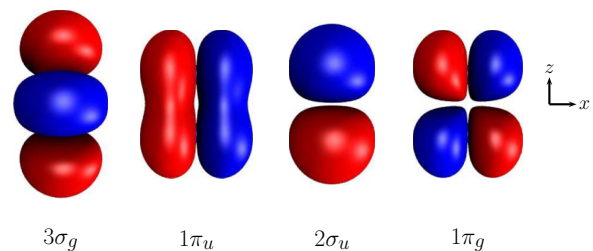
FIG. 8. Molecular orbitals involved in the two-electron flux density.

thus it is true that even when the nuclear motion plays a secondary role in the electronic flux density, the electrons still have information about the nuclear motion, at least in the predissociation region, i.e., at internuclear distance where the exchange of momentum between electrons and nuclei happens ($R = 2.4a_0$).

IV. SUMMARY

We have studied the predissociation of the $C\,^2\Sigma_u^{\,+}$ into the $B\,^2\Sigma_u^{\,+}$ state of the $N_2^{\,+}$ molecular ion by solving the Schrödinger equation. The predissociation is driven by the nonadiabatic coupling, i.e., by the coupling of the two electronic states through the kinetic energy operator of the nuclei. The predissociation rates were calculated accordingly to Fermi's golden rule and successfully compared with the reported experimental data [4,6], improving previous calculations [6]. The dynamics was studied in detail until 600 fs by calculation of the nuclear and electronic probability and flux densities. It was observed that during the first 100 fs, the probability of dissociation does not grow linearly as expected from Fermi's golden rule. The validity of this rule, resulting from the time-dependent perturbation theory to the first order approximation, turns out to be $2\pi\hbar/\min\{|E_a - E|,|E - E_b|\} \ll t \ll 2\pi\hbar\rho(E)$ [50]; for our case, the lower and upper limit is about 17 and 7×10^5 fs, respectively. Presumably, the failure beyond 17 fs is due to the strong coupling between the $C\,^2\Sigma_u^{\,+}$ and $B\,^2\Sigma_u^{\,+}$ vibrational wave packets, indicated by large oscillations of their populations until 100 fs. Afterwards, the population of the vibrational part of the $B\,^2\Sigma_u^{\,+}$ state becomes constant together with the linear grow of the population of its dissociative part. In other words, the break down of Fermi's golden rule is observed during the first 100 fs of the dynamics with its subsequent restoration. Interestingly, 100 fs seems to be a time window large enough for tracing the nonlinear predissociation process by means of time-resolved spectroscopy experiments. We also found a strong correlation between the electronic and nuclear motions by looking at the flux densities, both motions occurring in the femtosecond time scale. Such correlation was not observed in the dynamics of the polarized H_2 molecule [16], in which an electronic wave packet was induced by the action of a laser field. However, the dynamics of H_2 happens to be adiabatic, i.e., after the laser field, the two electronic states were not longer coupled. Particularly in the dynamics with $N_2^{\,+}$, the Bohr frequency $\omega_{mn} = (E_n - E_m)/\hbar$ for the electronic motion is of the order of the Bohr frequency for the nuclear motion, thus having similar periods the nuclear and electronic flux densities. In the dynamics with H_2 such Bohr frequencies were totally different, where for the electronic motion it was of the order of the energy gap between the electronic states, leading an electronic flux density varying in the attosecond time scale, much more faster than the nuclear flux density which varied in the femtosecond time scale. Fourier analysis of the nuclear probability and flux density was also performed. Such analysis allowed reconstruction of the potential energy curve of the $C\,^2\Sigma_u^{\,+}$ state but not of the $B\,^2\Sigma_u^{\,+}$ state. The reason is due to the nonadiabatic coupling, which causes an uncomplete scan of the potential energy curve $B\,^2\Sigma_u^{\,+}$ by its nuclear wave packet. Surprisingly, we found that, for the characterization of the

nuclear wave functions involved in the dynamics, the flux density seems to be more suitable than the nuclear probability density. We hope the framework presented here serves as a useful tool for studying the correlated electron-nuclear dynamics happening in different nonadiabatic scenarios of the diatomic molecules.

APPENDIX A: INTERFERING TERMS IN THE NUCLEAR PROBABILITY AND FLUX DENSITIES

We consider the probability density for the $B\,^2\Sigma_u^{\,+}$ state Eq. (22)

$$\rho_B(R,t) = \sum_{\mu_B \nu_B} c_{\mu_B}^*(t)c_{\nu_B}(t)\chi_{\mu_B}^*(R)\chi_{\nu_B}(R)e^{i(W_{\mu_B}-W_{\nu_B})t/\hbar}.$$

(A1)

The above summations on the vibrational quantum numbers μ_B and ν_B can be performed from 0 until K_b and then from $K_b + 1$ until N_B, with K_b the number of bound states and N_B the total number of states (bound and continuum). Thus Eq. (A1) can be rewritten as

$$\rho_B(R,t) = \rho_{B,\text{vib}}(R,t) + \rho_{B,\text{dis}}(R,t) + \Delta\rho_{B,\text{int}}(R,t), \quad (A2)$$

where

$$\rho_{B,\text{vib}}(R,t) = \sum_{\mu_B=0}^{K_b} \sum_{\nu_B=0}^{K_b} c_{\mu_B}^*(t)c_{\nu_B}(t)\chi_{\mu_B}^*(R)\chi_{\nu_B}(R)$$
$$\times e^{i(W_{\mu_B}-W_{\nu_B})t/\hbar} \quad (A3)$$

is the probability density associated to the vibrating $N_2^{\,+}$,

$$\rho_{B,\text{dis}}(R,t) = \sum_{\mu_B=K_b+1}^{N_B} \sum_{\nu_B=K_b+1}^{N_B} c_{\mu_B}^*(t)c_{\nu_B}(t)\chi_{\mu_B}^*(R)\chi_{\nu_B}(R)$$
$$\times e^{i(W_{\mu_B}-W_{\nu_B})t/\hbar} \quad (A4)$$

is the probability density associated to the dissociating $N_2^{\,+}$, and

$$\Delta\rho_{B,\text{int}}(R,t) = \sum_{\mu_B=0}^{K_b} \sum_{\nu_B=K_b+1}^{N_B} c_{\mu_B}^*(t)c_{\nu_B}(t)\chi_{\mu_B}^*(R)\chi_{\nu_B}(R)$$
$$\times e^{i(W_{\mu_B}-W_{\nu_B})t/\hbar}$$
$$+ \sum_{\mu_B=K_b+1}^{N_B} \sum_{\nu_B=0}^{K_b} c_{\mu_B}^*(t)c_{\nu_B}(t)\chi_{\mu_B}^*(R)\chi_{\nu_B}(R)$$
$$\times e^{i(W_{\mu_B}-W_{\nu_B})t/\hbar} \quad (A5)$$

is the interfering term between the vibrating and dissociating $N_2^{\,+}$. In a similar manner, the flux density (23) can be rewritten as

$$j_B(R,t) = j_{B,\text{vib}}(R,t) + j_{B,\text{dis}}(R,t) + \Delta j_{B,\text{int}}(R,t) \quad (A6)$$

with

$$j_{B,\text{vib}}(R,t) = \frac{\hbar}{iM} \sum_{\mu_B=0}^{K_b} \sum_{\nu_B=0}^{K_b} c_{\mu_B}^*(t) c_{\nu_B}(t) \chi_{\mu_B}^*(R)$$

$$\times \frac{d}{dR} \chi_{\nu_B}(R) e^{i(W_{\mu_B}-W_{\nu_B})t/\hbar}, \quad \text{(A7)}$$

$$j_{B,\text{dis}}(R,t) = \frac{\hbar}{iM} \sum_{\mu_B=K_b+1}^{N_B} \sum_{\nu_B=K_b+1}^{N_B} c_{\mu_B}^*(t) c_{\nu_B}(t) \chi_{\mu_B}^*(R)$$

$$\times \frac{d}{dR} \chi_{\nu_B}(R) e^{i(W_{\mu_B}-W_{\nu_B})t/\hbar}, \quad \text{(A8)}$$

and

$$\Delta j_{B,\text{int}}(R,t) = \frac{\hbar}{iM} \sum_{\mu_B=0}^{K_b} \sum_{\nu_B=K_b+1}^{N_B} c_{\mu_B}^*(t) c_{\nu_B}(t) \chi_{\mu_B}^*(R)$$

$$\times \frac{d}{dR} \chi_{\nu_B}(R) e^{i(W_{\mu_B}-W_{\nu_B})t/\hbar}$$

$$+ \frac{\hbar}{iM} \sum_{\mu_B=K_b+1}^{N_B} \sum_{\nu_B=0}^{K_b} c_{\mu_B}^*(t) c_{\nu_B}(t) \chi_{\mu_B}^*(R)$$

$$\times \frac{d}{dR} \chi_{\nu_B}(R) e^{i(W_{\mu_B}-W_{\nu_B})t/\hbar} \quad \text{(A9)}$$

the flux density associated to the vibrating and dissociating N_2^+ and the interfering term, respectively. The interfering terms $\Delta\rho_{\text{int}}(R,t)$ and $\Delta j_{\text{int}}(R,t)$ were analyzed in the H_2^+ system [28], where they were shown to be small corrections to the vibrating and dissociating part, the correction being much less noticeable in the flux density than in the probability density. Moreover they do not contribute to the integrated quantities since $\int dR\,\Delta\rho_{\text{int}}(R,t) = 0$ and $\int dR\,\Delta j_{\text{int}}(R,t) = 0$.

APPENDIX B: EXPECTATION VALUE OF THE TWO-ELECTRON FLUX DENSITY OPERATOR

The configuration interaction expansion for the molecular electronic states Ψ_n ($n = C,B$) is given by

$$\Psi_n(\mathbf{x}; R) = \sum_i C_{in}(R) \psi_i(\mathbf{x}; R), \quad \text{(B1)}$$

where ψ_i denotes a configuration. By substituting the last equation into Eq. (32) one can split the vector field $\mathbf{\Lambda}_{BC}(\mathbf{r}_1', \mathbf{r}_2'; R)$ into contributions between two configurations i and j:

$$\mathbf{\Lambda}_{BC}(\mathbf{r}_1', \mathbf{r}_2'; R) = \sum_{i,j>i} \lambda_{BC}^{ij}(\mathbf{r}_1', \mathbf{r}_2'; R), \quad \text{(B2)}$$

where

$$\lambda_{BC}^{ij}(\mathbf{r}_1', \mathbf{r}_2'; R) = F^{ij}(R)[\langle \psi_i(R)|\hat{j}(\mathbf{r}_1', \mathbf{r}_2')|\psi_j(R)\rangle$$

$$- \langle \psi_j(R)|\hat{j}(\mathbf{r}_1', \mathbf{r}_2')|\psi_i(R)\rangle] \quad \text{(B3)}$$

with

$$F^{ij}(R) = C_{iB}(R)C_{jC}(R) - C_{iC}(R)C_{jB}(R). \quad \text{(B4)}$$

Note that $\lambda_{BC}^{ij}(\mathbf{r}_1', \mathbf{r}_2'; R)$ is an imaginary quantity (Born-Oppenheimer molecular states Ψ_B and Ψ_C are real functions), and therefore $\mathbf{j}_{BC}^{\text{TEFD}}(\mathbf{r}_1', \mathbf{r}_2', t)$ is real as expected [see Eq. (31)]. Our goal is to calculate the functions $\lambda_{BC}^{ij}(\mathbf{r}_1', \mathbf{r}_2'; R)$. We will exemplify this for the case of $i = 1$ and $j = 2$. Using second quantization [51], we note that configurations ψ_1 and ψ_2 appearing in Eqs. (25) and (26) are related each other as follows (see Table I):

$$|\psi_2\rangle = a_{1\pi_g}^\dagger a_{1\pi_u} a_{2\bar{\sigma}_u}^\dagger a_{3\bar{\sigma}_g} |\psi_1\rangle, \quad \text{(B5)}$$

where the bar means a β-spin orbital and no bar means an α-spin orbital. The two-electron flux density operator $\hat{j}(\mathbf{r}_1', \mathbf{r}_2', t)$ in terms of the creation and annihilation operators reads

$$\hat{j}(\mathbf{r}_1', \mathbf{r}_2') = \frac{\hbar}{im_e} \sum_{ijkl} \langle ij|\delta(\mathbf{r}_1-\mathbf{r}_1')\delta(\mathbf{r}_2-\mathbf{r}_2')(\nabla_1+\nabla_2)|kl\rangle$$

$$\times a_i^\dagger a_j^\dagger a_k a_l. \quad \text{(B6)}$$

Thus by inserting Eqs. (B6) and (B5) into Eq. (B3) and using the anticommutation relations of the creation and annihilation operators, i.e., $\{a_i^\dagger, a_j^\dagger\} = a_i^\dagger a_j^\dagger + a_j^\dagger a_i^\dagger = 0$, $\{a_i, a_j\} = a_i a_j + a_j a_i = 0$ and $\{a_i, a_j^\dagger\} = a_i a_j^\dagger + a_j^\dagger a_i = \delta_{ij}$, one obtains

$$\lambda_{BC}^{12}(\mathbf{r}_1', \mathbf{r}_2'; R)$$

$$= \frac{\hbar F^{12}(R)}{im_e} \iint d\omega_1\, d\omega_2 \big[\phi_{3\bar{\sigma}_g}(\mathbf{r}_1'; R)\phi_{1\pi_u}(\mathbf{r}_2'; R)$$

$$\times (\overleftrightarrow{\nabla}_1 + \overleftrightarrow{\nabla}_2)\phi_{2\bar{\sigma}_u}(\mathbf{r}_1'; R)\phi_{1\pi_g}(\mathbf{r}_2'; R) - \phi_{1\pi_u}(\mathbf{r}_1'; R)\phi_{3\bar{\sigma}_g}$$

$$\times (\mathbf{r}_2'; R)(\overleftrightarrow{\nabla}_1 + \overleftrightarrow{\nabla}_2)\phi_{2\bar{\sigma}_u}(\mathbf{r}_1'; R)\phi_{1\pi_g}(\mathbf{r}_2'; R)$$

$$- \phi_{3\bar{\sigma}_g}(\mathbf{r}_1'; R)\phi_{1\pi_u}(\mathbf{r}_2'; R)(\overleftrightarrow{\nabla}_1 + \overleftrightarrow{\nabla}_2)\phi_{1\pi_g}$$

$$\times (\mathbf{r}_1'; R)\phi_{2\bar{\sigma}_u}(\mathbf{r}_2'; R) + \phi_{1\pi_u}(\mathbf{r}_1'; R)\phi_{3\bar{\sigma}_g}$$

$$\times (\mathbf{r}_2'; R)(\overleftrightarrow{\nabla}_1 + \overleftrightarrow{\nabla}_2)\phi_{1\pi_g}(\mathbf{r}_1'; R)\phi_{2\bar{\sigma}_u}(\mathbf{r}_2'; R)\big] \quad \text{(B7)}$$

with the short notation $\overleftrightarrow{\nabla} \equiv \overrightarrow{\nabla} - \overleftarrow{\nabla}$, and $\overrightarrow{\nabla}$ acting on the right side as the usual way, and $\overleftarrow{\nabla}$ acting on the left side. Now performing integrals over the spin coordinates (orbitals with bars are orthogonal to those one without bars) we get

$$\lambda_{BC}^{12}(\mathbf{r}_1', \mathbf{r}_2'; R)$$

$$= \frac{\hbar F^{12}(R)}{im_e} \big[\phi_{3\sigma_g}(\mathbf{r}_1'; R)\phi_{1\pi_u}(\mathbf{r}_2'; R)(\overleftrightarrow{\nabla}_1 + \overleftrightarrow{\nabla}_2)\phi_{2\sigma_u}$$

$$\times (\mathbf{r}_1'; R)\phi_{1\pi_g}(\mathbf{r}_2'; R) + \phi_{1\pi_u}(\mathbf{r}_1'; R)\phi_{3\sigma_g}(\mathbf{r}_2'; R)$$

$$\times (\overleftrightarrow{\nabla}_1 + \overleftrightarrow{\nabla}_2)\phi_{1\pi_g}(\mathbf{r}_1'; R)\phi_{2\sigma_u}(\mathbf{r}_2'; R)\big]. \quad \text{(B8)}$$

Molecular orbitals $\phi_i(\mathbf{r}; R)$ and their gradients $\nabla\phi_i(\mathbf{r}; R)$ can be obtained from the molecular wave function processing toolbox `orbkit` [52]. Equation (B8) can be rewritten in the

vector form as

$$\lambda_{BC}^{12}(\mathbf{r}_1',\mathbf{r}_2';R)$$

$$= \frac{\hbar F^{12}(R)}{im_e}$$

$$\times \begin{pmatrix} \phi_{1\pi_u}\phi_{1\pi_g}(\phi_{3\sigma_g}\overset{\leftrightarrow}{\nabla}_1\phi_{2\sigma_u}) + \phi_{3\sigma_g}\phi_{2\sigma_u}(\phi_{1\pi_u}\overset{\leftrightarrow}{\nabla}_1\phi_{1\pi_g}) \\ \phi_{3\sigma_g}\phi_{2\sigma_u}(\phi_{1\pi_u}\overset{\leftrightarrow}{\nabla}_2\phi_{1\pi_g}) + \phi_{1\pi_u}\phi_{1\pi_g}(\phi_{3\sigma_g}\overset{\leftrightarrow}{\nabla}_2\phi_{2\sigma_u}) \end{pmatrix},$$

(B9)

where the explicit dependence of the molecular orbitals on $\mathbf{r}_i'$ and R has been omitted for simplicity. Note that each row of Eq. (B9) is a six-component vector, i.e., $(\partial_{x_1},\partial_{y_1},\partial_{z_1})$ and $(\partial_{x_2},\partial_{y_2},\partial_{z_2})$, completing our six-dimensional vector field $\lambda_{BC}^{12}(\mathbf{r}_1',\mathbf{r}_2';R)$ for a given internuclear distance R.

FIG. 9. Weight functions $F^{ij}(R)$ that accompany the vector fields $\lambda_{BC}^{ij}(\mathbf{r}_1',\mathbf{r}_2';R)$.

APPENDIX C: EFFECT OF INCLUDING MORE CONFIGURATIONS IN THE TWO-ELECTRON FLUX DENSITY OPERATOR

To examine the effect of including more than the first two configurations of the CI wave function, we include ψ_3 in the TEFD as well. Following the steps of Appendix B we first express ψ_3 using second quantization operators

$$|\psi_3\rangle = a_{1\tilde{\pi}_g}^\dagger a_{1\pi_u} a_{2\tilde{\sigma}_u}^\dagger a_{3\tilde{\sigma}_g} |\psi_1\rangle, \tag{C1}$$

$$|\psi_3\rangle = a_{1\pi_u}^\dagger a_{1\pi_g} a_{1\tilde{\pi}_g}^\dagger a_{1\tilde{\pi}_u} |\psi_2\rangle \tag{C2}$$
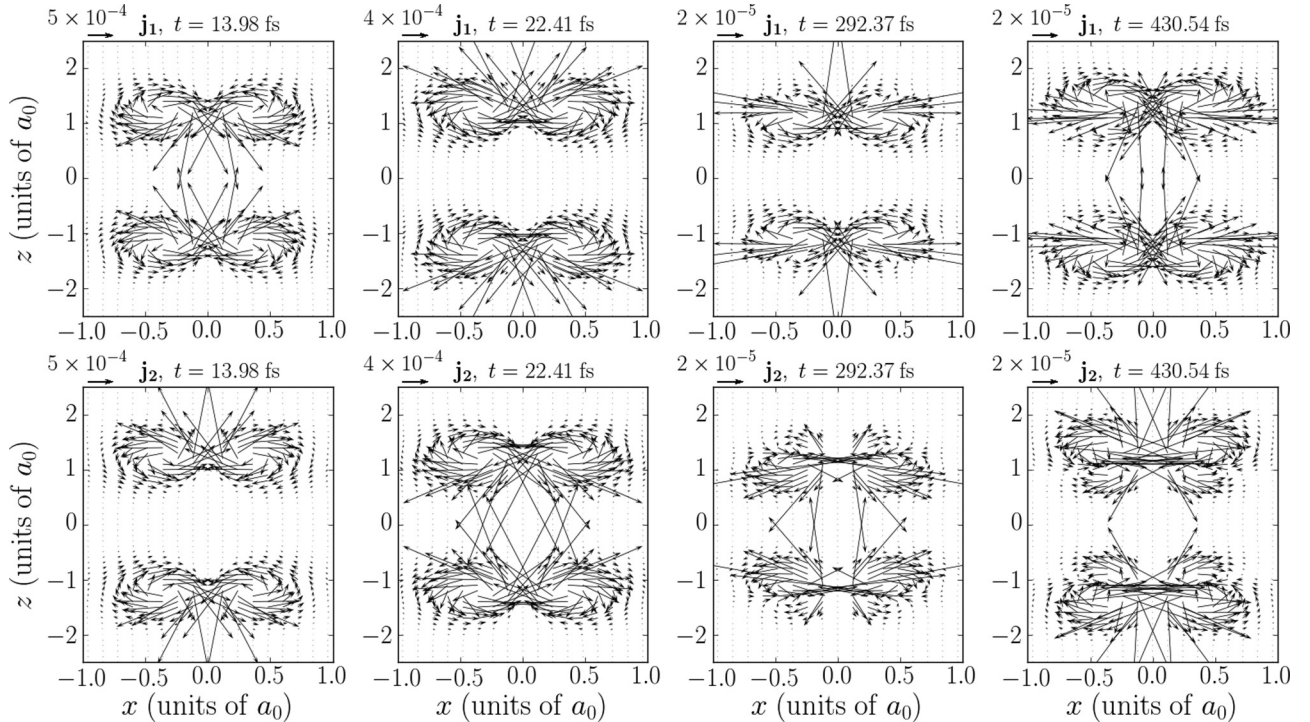
FIG. 10. Results for the two-electron flux density when including three configurations: $\mathbf{j}_{BC}^{\text{TEFD}}(\mathbf{r}_1,\mathbf{r}_2,t) = i \int dR \Lambda_{BC}(\mathbf{r}_1,\mathbf{r}_2;R) G_{BC}(R,t)$ with $\Lambda_{BC}(\mathbf{r}_1,\mathbf{r}_2;R) = \lambda_{BC}^{12}(\mathbf{r}_1,\mathbf{r}_2;R) + \lambda_{BC}^{13}(\mathbf{r}_1,\mathbf{r}_2;R) + \lambda_{BC}^{23}(\mathbf{r}_1,\mathbf{r}_2;R)$. The representation is the same as in Fig. 7, i.e., $\mathbf{j}_{BC}^{\text{TEFD}}(\mathbf{r}_1,\mathbf{r}_2,t) = (\mathbf{j}_1(\mathbf{r}_1,\mathbf{r}_2,t),\mathbf{j}_2(\mathbf{r}_1,\mathbf{r}_2,t))$ with $\mathbf{r}_1 = (x,y = 0,z)$ and $\mathbf{r}_2 = -\mathbf{r}_1$ at the four characteristic times: $t = 13.98$ fs, $t = 22.41$ fs, $t = 292.37$ fs, and $t = 430.54$ fs.

and insert it into Eq. (B3) to obtain

$$
\lambda_{BC}^{13}(\mathbf{r}_1',\mathbf{r}_2';R) = \frac{\hbar F^{13}(R)}{i m_e} \begin{pmatrix} \phi_{1\pi_u}\phi_{1\pi_g}(\phi_{3\sigma_g}\overset{\leftrightarrow}{\nabla}_1\phi_{2\sigma_u}) + \phi_{3\sigma_g}\phi_{2\sigma_u}(\phi_{1\pi_u}\overset{\leftrightarrow}{\nabla}_1\phi_{1\pi_g}) - \phi_{3\sigma_g}\phi_{1\pi_g}(\phi_{1\pi_u}\overset{\leftrightarrow}{\nabla}_1\phi_{2\sigma_u}) - \phi_{1\pi_u}\phi_{2\sigma_u}(\phi_{3\sigma_g}\overset{\leftrightarrow}{\nabla}_1\phi_{1\pi_g}) \\ \phi_{3\sigma_g}\phi_{2\sigma_u}(\phi_{1\pi_u}\overset{\leftrightarrow}{\nabla}_2\phi_{1\pi_g}) + \phi_{1\pi_u}\phi_{1\pi_g}(\phi_{3\sigma_g}\overset{\leftrightarrow}{\nabla}_2\phi_{2\sigma_u}) - \phi_{1\pi_u}\phi_{2\sigma_u}(\phi_{3\sigma_g}\overset{\leftrightarrow}{\nabla}_2\phi_{1\pi_g}) - \phi_{3\sigma_g}\phi_{1\pi_g}(\phi_{1\pi_u}\overset{\leftrightarrow}{\nabla}_2\phi_{2\sigma_u}) \end{pmatrix}
$$

$$(C3)$$

and

$$
\lambda_{BC}^{23}(\mathbf{r}_1',\mathbf{r}_2';R) = \frac{2\hbar F^{23}(R)}{i m_e} \begin{pmatrix} \phi_{1\pi_g}\phi_{1\pi_u}(\phi_{1\pi_u}\overset{\leftrightarrow}{\nabla}_1\phi_{1\pi_g}) \\ \phi_{1\pi_u}\phi_{1\pi_g}(\phi_{1\pi_g}\overset{\leftrightarrow}{\nabla}_2\phi_{1\pi_u}) \end{pmatrix}. \quad (C4)
$$

In Fig. 9 we compare the three weight functions $F^{ij}(R)$ of interest. As expected, the main contribution is due to $F^{12}(R)$ arising from the two main configuration ψ_1 and ψ_2. Comparing the TEFD in Figs. 7 and 10, we see that the shape remains unaffected and only the magnitude changes.

APPENDIX D: DISTANT-DEPENDENT TOTAL ENERGIES AND NONADIABATIC COUPLING MATRIX ELEMENTS

Table III collects energies and non-adiabatic couplings as a function of the internuclear distance calculated at the MRCI-SD/aug-cc-pV5Z level.

TABLE III. Potential energy curves and non-adiabatic coupling (values close to zero are omitted) for $B\,^2\Sigma_u^+$ and $C\,^2\Sigma_u^+$ electronic states. Results obtained on the MRCI-SD/aug-cc-pV5Z level.

R [a_0]	$B\,^2\Sigma_u^+$ [$E_{\rm h}$]	$C\,^2\Sigma_u^+$ [$E_{\rm h}$]	$T_{mn}^{(1)}$	$\frac{d}{dR}T_{mn}^{(1)}$
1.63	−108.477 160	−107.907 986	0.19	0.40
1.66	−108.530 265	−107.995 551	0.21	0.45
1.70	−108.574 509	−108.072 876	0.23	0.50
1.74	−108.610 966	−108.141 055	0.25	0.57
1.78	−108.640 587	−108.201 066	0.27	0.65
1.81	−108.664 219	−108.253 780	0.30	0.74
1.85	−108.682 612	−108.299 971	0.33	0.84
1.89	−108.696 434	−108.340 332	0.36	0.96
1.93	−108.706 280	−108.375 478	0.40	1.11
1.97	−108.712 683	−108.405 957	0.44	1.28
2.00	−108.716 120	−108.432 258	0.50	1.48
2.04	−108.717 019	−108.454 811	0.56	1.72
2.08	−108.715 767	−108.473 999	0.63	2.00
2.12	−108.712 717	−108.490 157	0.71	2.31
2.15	−108.708 189	−108.503 579	0.80	2.66
2.19	−108.702 480	−108.514 515	0.91	3.03
2.23	−108.695 867	−108.523 182	1.03	3.39
2.27	−108.688 609	−108.529 759	1.16	3.69
2.31	−108.680 950	−108.534 393	1.31	3.83
2.34	−108.673 120	−108.537 204	1.45	3.73
2.38	−108.665 331	−108.538 263	1.58	3.26
2.42	−108.657 760	−108.537 641	1.69	2.36
2.46	−108.650 582	−108.535 569	1.76	1.08
2.53	−108.637 751	−108.527 315	1.73	−1.78
2.57	−108.632 158	−108.521 442	1.64	−2.88
2.61	−108.627 080	−108.514 652	1.52	−3.55
2.65	−108.622 457	−108.507 451	1.38	−3.82

TABLE III. (*Continued.*)

R [a_0]	$B\,^2\Sigma_u^+$ [$E_{\rm h}$]	$C\,^2\Sigma_u^+$ [$E_{\rm h}$]	$T_{mn}^{(1)}$	$\frac{d}{dR}T_{mn}^{(1)}$
2.72	−108.614 297	−108.490 695	1.09	−3.54
2.76	−108.610 633	−108.482 085	0.97	−3.21
2.80	−108.607 177	−108.473 398	0.85	−2.84
2.83	−108.603 892	−108.464 739	0.75	−2.48
2.87	−108.600 747	−108.456 198	0.66	−2.14
2.91	−108.597 722	−108.447 846	0.59	−1.85
2.95	−108.594 800	−108.439 746	0.52	−1.59
2.99	−108.591 970	−108.431 950	0.47	−1.38
3.02	−108.589 223	−108.424 515	0.42	−1.19
3.06	−108.586 553	−108.417 513	0.38	−1.03
3.10	−108.583 954	−108.411 069	0.34	−0.90
3.14	−108.581 421	−108.405 435	0.31	−0.78
3.17	−108.578 948	−108.401 125	0.28	−0.69
3.21	−108.576 526	−108.399 021	0.26	−0.61
3.25	−108.574 147	−108.400 025	0.24	−0.53
3.29	−108.571 806	−108.403 970	0.22	−0.47
3.33	−108.569 508	−108.409 288	0.20	−0.42
3.36	−108.567 269	−108.414 422	0.19	−0.38
3.40	−108.565 095	−108.418 788	0.17	−0.34
3.44	−108.562 986	−108.422 418	0.16	−0.30
3.48	−108.560 940	−108.425 484	0.15	−0.27
3.51	−108.558 951	−108.428 128	0.14	−0.25
3.55	−108.557 018	−108.430 445	0.13	−0.23
3.59	−108.555 138	−108.432 492	0.12	−0.20
3.63	−108.553 309	−108.434 306	0.11	−0.19
3.67	−108.551 530	−108.435 914	0.11	−0.17
3.70	−108.549 798	−108.437 335	0.10	−0.16
3.74	−108.548 112	−108.438 585	0.10	−0.14
3.78	−108.546 472	−108.439 681	0.09	−0.13
3.82	−108.544 880	−108.440 722	0.09	−0.12
3.86	−108.543 330	−108.441 538	0.08	−0.11
3.89	−108.541 823	−108.442 235	0.08	−0.10
3.93	−108.540 359	−108.442 821	0.07	−0.10
3.97	−108.538 937	−108.443 305	0.07	−0.09
4.01	−108.537 556	−108.443 695	0.07	−0.08
4.04	−108.536 217	−108.443 997	0.06	−0.08
4.08	−108.534 917	−108.444 219	0.06	−0.07
4.12	−108.533 658	−108.444 367	0.06	−0.07
4.16	−108.532 438	−108.444 447	0.06	−0.06
4.20	−108.531 257	−108.444 463	0.05	−0.06
4.23	−108.530 115	−108.444 422	0.05	−0.06
4.27	−108.529 010	−108.444 265	0.05	−0.05
4.31	−108.527 943	−108.443 919	0.05	−0.05
4.35	−108.526 913	−108.444 000	0.04	−0.05
4.38	−108.525 920	−108.443 773	0.04	−0.04
4.42	−108.524 962	−108.443 510	0.04	−0.04

TABLE III. (*Continued.*)

R [a_0]	$B\,^2\Sigma_u^+$ [E_h]	$C\,^2\Sigma_u^+$ [E_h]	$T_{mn}^{(1)}$	$\frac{d}{dR}T_{mn}^{(1)}$
4.46	−108.524 040	−108.443 214	0.04	−0.04
4.50	−108.523 152	−108.442 887	0.04	−0.04
4.54	−108.522 300	−108.442 533	0.04	−0.04
4.57	−108.521 481	−108.442 155	0.04	−0.03
4.61	−108.520 696	−108.441 755	0.03	−0.03
4.65	−108.519 943	−108.441 335	0.03	−0.03
4.69	−108.519 223	−108.440 897	0.03	−0.03
4.72	−108.518 534	−108.440 444	0.03	−0.03
4.76	−108.517 876	−108.439 978	0.03	−0.03
4.80	−108.517 247	−108.439 500	0.03	−0.02
4.84	−108.516 647	−108.439 014	0.03	−0.02
4.88	−108.516 074	−108.438 520	0.03	−0.02
4.91	−108.515 529	−108.438 021	0.03	−0.02
4.99	−108.514 515	−108.437 011	0.03	−0.02
5.03	−108.514 046	−108.436 502	0.02	−0.02
5.06	−108.513 602	−108.435 990	0.02	−0.02
5.10	−108.513 181	−108.435 474	0.02	−0.02
5.14	−108.512 783	−108.434 956	0.02	−0.02
5.18	−108.512 408	−108.434 435	0.02	−0.02
5.22	−108.512 053	−108.433 914	0.02	−0.02
5.25	−108.511 716	−108.433 398	0.02	−0.01
5.29	−108.511 398	−108.432 889	0.02	−0.01
5.33	−108.511 096	−108.432 388	0.02	−0.01
5.37	−108.510 811	−108.431 894	0.02	−0.01
5.40	−108.510 542	−108.431 406	0.02	−0.01
5.44	−108.510 289	−108.430 923	0.02	−0.01
5.48	−108.510 050	−108.430 442	0.02	−0.01
5.52	−108.509 825	−108.429 962	0.02	−0.01
5.56	−108.509 614	−108.429 480	0.02	−0.01

TABLE III. (*Continued.*)

R [a_0]	$B\,^2\Sigma_u^+$ [E_h]	$C\,^2\Sigma_u^+$ [E_h]	$T_{mn}^{(1)}$	$\frac{d}{dR}T_{mn}^{(1)}$
5.59	−108.509 415	−108.428 989	0.02	−0.01
5.63	−108.509 228	−108.428 482	0.02	−0.01
5.67	−108.509 053	−108.427 946	0.02	−0.01
6.05	−108.507 948	−108.424 392	0.01	−0.01
6.43	−108.507 447	−108.422 703	0.01	−0.01
6.80	−108.507 275	−108.421 854	0.01	0.00
7.37	−108.507 255	−108.420 549	–	–
7.94	−108.507 454	−108.419 472	–	–
8.50	−108.507 482	−108.418 641	–	–
9.07	−108.507 479	−108.418 048	–	–
9.64	−108.507 457	−108.417 638	–	–
10.20	−108.507 425	−108.417 358	–	–
10.77	−108.507 390	−108.417 165	–	–
11.34	−108.507 355	−108.417 031	–	–
11.91	−108.507 323	−108.416 936	–	–
12.47	−108.507 295	−108.416 867	–	–
15.12	−108.507 201	−108.416 709	–	–
17.01	−108.507 169	−108.416 664	–	–
18.90	−108.507 150	−108.416 639	–	–
20.79	−108.507 139	−108.416 623	–	–
22.68	−108.507 132	−108.416 613	–	–
24.57	−108.507 128	−108.416 606	–	–
26.46	−108.507 124	−108.416 601	–	–
28.35	−108.507 122	−108.416 597	–	–
41.57	−108.507 110	−108.416 586	–	–
52.91	−108.507 109	−108.416 584	–	–
60.47	−108.507 109	−108.416 583	–	–
69.92	−108.507 108	−108.416 583	–	–
86.93	−108.507 108	−108.416 583	–	–
94.49	−108.507 108	−108.416 583	–	–

[1] C. A. van de Runstraat, F. J. de Heer, and T. R. Goovers, Excitation and decay of the $C\,^2\Sigma_u^+$ state of N_2^+ in the case of electron impact on N_2, Chem. Phys. **3**, 431 (1974).

[2] R. Marx, G. Mauclaire, and S. Fenistein, On the mechanism of the $He^+ + N_2$ thermal dissociative charge transfer reaction, Chem. Phys. Lett. **33**, 357 (1975).

[3] T. R. Govers, C. A. van de Runstraat, and F. J. Heer, Excitation and decay of the $C\,^2\Sigma_u^+$ state of N_2^+ following collisions of He^+ ions with N_2 isotopes, Chem. Phys. **9**, 285 (1975).

[4] P. Erman, Direct measurements of the N_2^+C state predissociation probability, Phys. Scr. **14**, 51 (1976).

[5] T. R. Govers, F. C. Fehsenfeld, D. L. Albritton, P. G. Fournier, and J. Fournier, Molecular isotope effects in the thermal-energy charge exchange between He^+ and N_2, Chem. Phys. Lett. **26**, 134 (1974).

[6] A. L. Roche and J. Tellinghuisen, Predissociation and perturbations in the $C\,^2\Sigma_u^+$ state of N_2^+ from interaction with the $B\,^2\Sigma_u^+$ state, Mol. Phys. **38**, 129 (1979).

[7] D. Strasser, L. H. Haber, B. Doughty, and S. R. Leone, Ultrafast predissociation of superexcited nitrogen molecules, Mol. Phys. **106**, 275 (2008).

[8] M. Lucchini, K. Kim, F. Calegari, F. Kelkensberg, W. Siu, G. Sansone, M. J. J. Vrakking, M. Hochlaf, and M. Nisoli,

Autoionization and ultrafast relaxation dynamics of highly excited states in N_2, Phys. Rev. A **86**, 043404 (2012).

[9] T. Frohnmeyer and T. Baumert, Femtosecond pump-probe photoelectron spectroscopy on Na_2: A tool to study basic coherent control schemes, Appl. Phys. B **71**, 259 (2000).

[10] T. Ergler, A. Rudenko, B. Feuerstein, K. Zrost, C. D. Schröter, R. Moshammer, and J. Ullrich, Spatiotemporal Imaging of Ultrafast Molecular Motion: Collapse and Revival of the D_2^+ Nuclear Wave Packet, Phys. Rev. Lett. **97**, 193001 (2006).

[11] J. Manz, J. F. Pérez-Torres, and Y. Yang, Nuclear Flux Densities in Diatomic Molecules Deduced from High-Resolution Pump-Probe Spectra with Spatiotemporal Resolutions down to 5 pm and 200 asec, Phys. Rev. Lett. **111**, 153004 (2013).

[12] D. J. Diestler, A. Kenfack, J. Manz, B. Paulus, J. F. Pérez-Torres, and V. Pohl, Computation of the electronic flux density in the Born-Oppenheimer approximation, J. Phys. Chem. A **117**, 8519 (2013).

[13] J. F. Pérez-Torres, Electronic flux densities in vibrating H_2^+ in terms of vibronic eigenstates, Phys. Rev. A **87**, 062512 (2013).

[14] V. Pohl and J. C. Tremblay, Born-Oppenheimer broken symmetry approach to electron flux density, Phys. Rev. A **93**, 012504 (2016).

[15] A. Schild, F. Agostini, and E. K. U. Gross, Electronic flux density beyond the Born-Oppenheimer approximation, J. Phys. Chem. A **120**, 3316 (2016).

[16] G. Hermann, B. Paulus, J. F. Pérez-Torres, and V. Pohl, Electronic and nuclear flux densities in the H_2 molecule, Phys. Rev. A **89**, 052504 (2014).

[17] T. B. Freedman, X. Gao, M.-L. Shih, and L. A. Nafie, Electron transition current density in molecules. 2. Ab initio calculations for electronic transitions in ethylene and formaldehyde, J. Phys. Chem. A **102**, 3352 (1998).

[18] M. Okuyama and K. Takatsuka, Electron flux in molecules induced by nuclear motion, Chem. Phys. Lett. **476**, 109 (2009).

[19] T. Gomez, G. Hermann, X. Zarate, J. F. Pérez-Torres, and J. C. Tremblay, Imaging the ultrafast photoelectron transfer process in alizarin-TiO_2, Molecules **20**, 13830 (2015).

[20] H. Bachau, E. Cormier, P. Decleva, J. E. Hansen, and F. Martín, Applications of B-splines in atomic and molecular physics, Rev. Prog. Phys. **64**, 1815 (2001).

[21] C. de Boor, *A Practical Guide to Splines* (Springer, New York, 1978).

[22] P. A. M. Dirac, The quantum theory of the emission and absorption of radiation, Proc. R. Soc. London A **114**, 243 (1927).

[23] T. Bredtmann, D. J. Diestler, S.-D. Li, J. Manz, J. F. Pérez-Torres, W.-J. Tian, Y.-B. Wu, Y. Yang, and H.-J. Zhai, Quantum theory of concerted electronic and nuclear fluxes associated with adiabatic intramolecular processes, Phys. Chem. Chem. Phys. **17**, 29421 (2015).

[24] C. A. Coulson and A. H. Neilson, Electron correlation in the ground state of helium, Proc. Phys. Soc. **78**, 831 (1961).

[25] R. J. Boyd, C. Sarasola, and J. Ugalde, Intraclude densities and electron correlation in the hydrogen molecule, J. Phys. B **21**, 2555 (1988).

[26] J. P. Restrepo Cuartas and J. L. Sanz-Vicario, Information and entanglement measures applied to the analysis of complexity in double excited states of helium, Phys. Rev. A **91**, 052301 (2015).

[27] A. Derevianko, E. Luc-Koenig, and F. Masnou-Seeuws, Application of B-splines in determining the eigenspectrum of diatomic molecules: Robust numerical description of halo-state and Feshbach molecules, Can. J. Phys. **87**, 67 (2009).

[28] J. F. Pérez-Torres, Dissociating $H_2^+(^2\Sigma_g^+, JM = 00)$ Ion as an exploding quantum bubble, J. Phys. Chem. A **119**, 2895 (2015).

[29] P. J. Knowles and H.-J. Werner, An efficient second-order MC SCF method for long configuration expansions, Chem. Phys. Lett. **115**, 259 (1985).

[30] H.-J. Werner and P. J. Knowles, An efficient internally contracted multiconfiguration-reference configuration interaction method, J. Chem. Phys. **89**, 5803 (1988).

[31] P. J. Knowles and H.-J. Werner, An efficient method for the evaluation of coupling coefficients in configuration interaction calculations, Chem. Phys. Lett. **145**, 514 (1988).

[32] H.-J. Werner, P. J. Knowles, G. Knizia, F. R. Manby, M. Schütz *et al.*, MOLPRO, version 2012.1 (2012).

[33] A. L. Roche and H. Lefebvre-Brion, Some ab initio calculations related to the predissociation of the $C\,^2\Sigma_u^+$ state of N_2^+, Chem. Phys. Lett. **32**, 155 (1975).

[34] S. R. Langhoff, C. W. Bauschlicher, and H. Partridge, Theoretical study of the N_2^+ Meinel system, J. Chem. Phys. **87**, 4716 (1987).

[35] S. R. Langhoff and C. W. Bauschlicher, Theoretical study of the first and second negative systems of N_2^+, J. Chem. Phys. **88**, 329 (1988).

[36] H. Liu, D. Shi, S. Wang, J. Sun, and Z. Zhu, Theoretical spectroscopy calculations on the 25 Λ-S and 66 Ω states of N_2^+ cation in the gas phase included the spin-orbit coupling effect, J. Quantum Spectrosc. Radiat. Transfer **147**, 207 (2014).

[37] R. A. Kendall, T. H. Dunning, and R. J. Harrison, Electron affinities of the first-row atoms revisited. Systematic basis sets and wave functions, J. Chem. Phys. **96**, 6796 (1992).

[38] D. J. Diestler, Coupled-channels quantum theory of electronic flux density in electronically adiabatic processes: Fundamentals, J. Phys. Chem. A **116**, 2728 (2012).

[39] D. J. Diestler, A. Kenfack, J. Manz, and B. Paulus, Coupled-channels quantum theory of electronic flux density in electronically adiabatic processes: Application to the hydrogen molecule ion, J. Phys. Chem. A **116**, 2736 (2012).

[40] S. Patchkovskii, Electronic currents and Born-Oppenheimer molecular dynamics, J. Chem. Phys. **137**, 084109 (2012).

[41] D. J. Tannor, *Introduction to Quantum Mechanics: A Time-Dependent Perspective* (University Science Books, Sausalito, CA, 2006).

[42] T. Bredtmann, H. Katsuki, J. Manz, K. Ohmori, and C. Stemmle, Wavepacket interferometry for nuclear densities and flux densities, Mol. Phys. **111**, 1691 (2013).

[43] A. Rudenko, T. Ergler, B. Feuerstein, K. Zrost, C. D. Schröter, R. Moshammer, and J. Ullrich, Real-time observation of vibrational revival in the fastest molecular system, Chem. Phys. **329**, 193 (2006).

[44] B. Feuerstein, T. Ergler, A. Rudenko, K. Zrost, C. D. Schröter, R. Moshammer, J. Ullrich, T. Niederhausen, and U. Thumm, Complete characterization of molecular dynamics in ultrashort laser fields, Phys. Rev. Lett. **99**, 153002 (2007).

[45] M. J. J. Vrakking, D. M. Villeneuve, and A. Stolow, Observation of fractional revivals of a molecular wave packet, Phys. Rev. A **54**, R37 (1996).

[46] E. Schrödinger, Quantisierung als Eigenwertproblem (Vierte Mitteilung), Ann. Phys. (Leipzig) **386**, 109 (1926).

[47] U. Thumm, T. Niederhausen, and B. Feuerstein, Time-series analysis of vibrational nuclear wave-packet dynamics in D_2^+, Phys. Rev. A **77**, 063401 (2008).

[48] M. Magrakvelidze, A. Kramer, K. Bartschat, and U. Thumm, Complementary imaging of the nuclear dynamics in laser-excited diatomic molecular ions in the time and frequency domains, J. Phys. B **47**, 124003 (2014).

[49] J. F. Pérez-Torres, Fourier analysis of the nuclear flux density in diatomic molecules: A complementary tool to map potential-energy curves and to characterize vibrational wave functions, Phys. Rev. A **91**, 022510 (2015).

[50] G. Baym, *Lectures on Quantum Mechanics* (Westview Press, Boulder, 1990).

[51] A. Szabo and N. S. Ostlund, *Modern Quantum Chemistry* (Dover Publications, New York, 1996).

[52] G. Hermann, V. Pohl, J. C. Tremblay, B. Paulus, H.-C. Hege, and A. Schild, ORBKIT: A modular Phyton toolbox for cross-platform post-processing of quantum chemical wavefunction data, J. Comput. Chem. **37**, 1511 (2016).